



Modelling H₂ and its effects on star formation using a joint implementation of GADGET-3 and KROME

Emanuel Sillero ¹★, Patricia B. Tissera ^{2,3}★, Diego G. Lambas,¹★ Stefano Bovino,⁴ Dominik R. Schleicher,⁴ Tommaso Grassi,^{5,6} Gustavo Bruzual⁷ and Stéphane Charlot⁸

¹*Instituto de Astronomía Teórica y Experimental (CONICET-UNC), Laprida 925, Córdoba, C.P. X5000BGR, Argentina*

²*Instituto de Astrofísica, Pontificia Universidad Católica, Av. Vicuña Mackenna 4860, Santiago, C.P. 8940000, Chile*

³*Centro de Astro-Ingeniería, Pontificia Universidad Católica de Chile, Av. Vicuña Mackenna 4860, Santiago, C.P. 8940000, Chile*

⁴*Departamento de Astronomía, Facultad Ciencias Físicas y Matemáticas, Universidad de Concepción, Av. Esteban Iturra s/n Barrio Universitario, Casilla 160-C, Concepción, Chile*

⁵*Universitäts-Sternwarte München, Scheinerstr. 1, D-81679 München, Germany*

⁶*Excellence Cluster Origin and Structure of the Universe, Boltzmannstr 2, D-85748 Garching bei München, Germany*

⁷*Instituto de Radioastronomía y Astrofísica, UNAM, Campus Morelia, Michoacán, C.P. 58089, México*

⁸*CNRS, UMR7095, Institut d'Astrophysique de Paris, Sorbonne Université, F-75014 Paris, France*

Accepted 2021 April 7. Received 2021 April 1; in original form 2020 June 4

ABSTRACT

We present P-GADGET3-K, an updated version of GADGET-3, that incorporates the chemistry package KROME. P-GADGET3-K follows the hydrodynamical and chemical evolution of cosmic structures, incorporating the chemistry and cooling of H₂ and metal cooling in non-equilibrium. We performed different runs of the same ICs to assess the impact of various physical parameters and prescriptions, namely gas metallicity, molecular hydrogen formation on dust, star formation recipes including or not H₂ dependence, and the effects of numerical resolution. We find that the characteristics of the simulated systems, both globally and at kpc-scales, are in good agreement with several observable properties of molecular gas in star-forming galaxies. The surface density profiles of star formation rate (SFR) and H₂ are found to vary with the clumping factor and resolution. In agreement with previous results, the chemical enrichment of the gas component is found to be a key ingredient to model the formation and distribution of H₂ as a function of gas density and temperature. A star formation algorithm that takes into account the H₂ fraction together with a treatment for the local stellar radiation field improves the agreement with observed H₂ abundances over a wide range of gas densities and with the molecular Kennicutt–Schmidt law, implying a more realistic modelling of the star formation process.

Key words: methods: numerical – ISM: molecules – galaxies: evolution – galaxies: ISM.

1 INTRODUCTION

The presence of molecular hydrogen (H₂), the most common molecule in the Universe (Herbst 2001), extends to a wide range of scales in galaxies and is essential for cooling the interstellar medium (ISM; Glover & Abel 2008). At pc-scales, the higher density regions protect molecules from being destroyed, enabling the formation of giant molecular clouds (GMCs). In the Milky Way, the GMC mass distribution follows a power law similar to that of the luminosity distribution of OB stars (Williams & McKee 1997), while their velocity dispersion obeys a power law that increases with the GMCs size (Larson 1981). Meanwhile, observations of nearby galaxies on kpc-scales show that the H₂ surface density correlates with the star formation rate (SFR; Bigiel et al. 2008; Schrubba et al. 2011; Leroy et al. 2013).

Schmidt, Wilson & Observatories (1959), from an analysis in the solar neighbourhood, and Kennicutt (1998), from a study to external galaxies, demonstrate that the neutral hydrogen surface density correlates with the SFR surface density (KS law). However, new measurements, which resolved the structure of external galaxies and the H₂ within them (e.g. Bigiel et al. 2008), find a tighter correlation between H₂ and SFR (the so-called molecular KS law). Although Leroy et al. (2013) confirm this trend and observations agree that cold and dense GMCs are associated with young and hot stars and active star formation (e.g. Genzel & Stutzki 1989), recent surveys of more than a thousand galaxies report a weak correlation between the total H₂ content and the SFR (Saintonge et al. 2017; Catinella et al. 2018). Hence, it is not yet clear if there is causal connection behind the correlation between H₂ content and star formation activity (SF). Unfortunately, H₂ is challenging to detect directly through observations owing to its lack of a dipole moment. This leads to CO measures to infer the amount of H₂ and identify the GMCs (Solomon et al. 1987). The H₂ abundance can then be estimated by applying a conversion factor, X_{CO}, between the CO

* E-mail: esillero@oac.unc.edu.ar (ES); tissera.patriciab@gmail.com (PBT); diego.garcia.lambas@gmail.com (DGL)

intensity and the H_2 column density. This conversion factor has been extensively measured and is found to be approximately constant for the Milky Way, $X_{\text{CO}} \approx 2 \times 10^{20} \text{ cm}^{-2} \text{ K}^{-1} \text{ km}^{-1} \text{ s}$ (Solomon et al. 1987; Strong & Mattox 1996; Dame, Hartmann & Thaddeus 2001; Goldsmith et al. 2008; Pineda et al. 2010). However, studies beyond the Milky Way show that it might depend on galaxy morphology and metallicity (Bolatto, Wolfire & Leroy 2013). The determination of the conversion factor is key to estimate the H_2 content as a function of time.

There are two channels for the formation of H_2 in the ISM: through exothermic synthesis reactions in the gas phase or catalysis by dust surface. The former are slow processes which were only important in the early Universe when heavy chemical elements were scarce (Galli & Palla 1998). The later is the more probable formation channel and is based on the use of interstellar dust grains as catalysts by which H I sticks and coalesces into H_2 in a more efficient way (Wakelam et al. 2017). Collisions at high temperatures ($T \sim 1000 \text{ K}$; Glover & Abel 2008) and ionization by high-energy photons ($h\nu \geq 15.42 \text{ eV}$; Abel et al. 1997) can dissociate H_2 . Additionally, photons with energy that falls into the Lyman–Werner (LW) band (11.2–13.6 eV) also dissociate H_2 . The GMCs can absorb the LW photons at stronger wavelengths forming a H I protective layer, while weaker wavelengths can penetrate towards the inner regions until they are also absorbed.

Two processes shield H_2 from radiation, the shielding by dust, and the H_2 self-shielding. The absorption rate is highly dependent on the wavelength of the LW band and only about 10 per cent of the LW absorption leads to H_2 dissociation (Stecher & Williams 1967). The rest of the absorbed photons do not contribute to photodissociation (Sternberg et al. 2014). On the other hand, the H_2 self-shielding is weak at low-column densities and increases further into the cloud.

The era of increasing precision for H_2 measurement requires a similar increase in sophistication for modelling the physics of the interstellar medium and H_2 chemistry in cosmological simulations. The past decade has seen a number of methods to model the H_2 chemistry in both semi-analytical galaxy models and hydrodynamical simulations of galaxy formation. Semi-analytical models use equilibrium equations to find the H_2 fraction under the assumption that the chemistry in each volume element is in an equilibrium state determined by purely local variables [e.g. McKee & Krumholz (2010) – KMT model]. On the other hand, hydrodynamic simulations use either equilibrium equations (e.g. Robertson & Kravtsov 2008; Kuhlen et al. 2012; Hopkins et al. 2014) or a series of non-equilibrium chemical networks (e.g. Richings & Schaye 2016a; Lupi et al. 2018). Equilibrium calculations have the advantage of being faster using the assumption that the chemical species are in equilibrium with their environment. Non-equilibrium codes instead, use local rates of destruction and creation of chemical species, and networks of rate equations to track locally atomic and molecular hydrogen in their galaxy simulations, together with the thermal evolution. Krumholz & Gnedin (2011) compared both kind of models, showing that they diverge at low metallicities. Non-equilibrium models are capable of preserving H_2 at lower densities (Tomassetti et al. 2014), producing clumpier H_2 mass distributions and star-forming regions closer to the KS law (Pallottini et al. 2017). Several works have been reported based on non-equilibrium schemes. Richings & Schaye (2016b) adapt the network developed by Richings, Schaye & Oppenheimer (2014a, b) for a version of GADGET-3 (Springel 2005). These authors use a fixed metallicity through out the entire simulation as in Nickerson, Teyssier & Rosdahl (2019). Hu et al. (2016, 2017) adapt the Glover & Clark (2012) network for GADGET-3 and also model metal production by SNaE. They track six species (H_2 , H II, CO, H I,

C II, and O I), of which only the first three are computed explicitly using the chemical network. Other authors resorted to the chemistry package KROME (Grassi et al. 2014), which can solve the chemical rate equations for any given reactions network, and also includes many other processes that are tightly connected to astrochemistry. Particularly, KROME allows to add thermal processes (as cooling from endothermic reactions and from several atoms and molecules, and heating from exothermic chemical reactions and photochemistry) considering, among others factors, the metal enrichment and a radiation field. Several works have implemented this package in hydrodynamical cosmological codes as RAMSES (Pallottini et al. 2017), GASOLINE2 (Capelo et al. 2018), and GIZMO (Lupi et al. 2018). These works assume different spatial uniform initial metallicity for the simulated galaxy.

Overall, the adopted chemical networks for the formation and destruction of H_2 are similar in all the mentioned works. They differ principally in how they model the synthesis of H_2 by dust grains. The first option is whether to include a clumping factor to account for unresolved dense structures in molecular clouds. The clumping factor enhances the formation of H_2 by some factor. The most common option is to adopt a constant factor (Christensen et al. 2012; Capelo et al. 2018). However, Micic et al. (2012) find that this may lead to an overproduction of H_2 in high-density regions. Instead, several works explore variable clumping factors. For example, Tomassetti et al. (2014) report that their model with the constant factor is closer to an equilibrium model (KMT) compared to the variable factor. Lupi et al. (2018) find that, depending on the gas properties, the clumping factor can vary significantly in their simulation, from 1 to $\sim 10^3$, but its distribution is far from being uniform. Several authors choose not to consider a clumping factor (Hu et al. 2016; Richings & Schaye 2016b; Pallottini et al. 2017; Nickerson, Teyssier & Rosdahl 2018).

The second option is whether to link the SFR explicitly to the H_2 content. Observations show that SF is correlated to H_2 (McKee & Ostriker 2007), but this may be because both stars and H_2 form in dense and cold environments and not because H_2 directly triggers SF (Glover & Clark 2012). Gnedin & Kravtsov (2011) argue that setting the SFR proportional to the H_2 density avoids possibly arbitrary density and temperature thresholds since H_2 naturally correlates with dense, cold gas (also Christensen et al. 2012; Tomassetti et al. 2014; Pallottini et al. 2017). However, Richings & Schaye (2016b), Hu et al. (2016), Capelo et al. (2018), Lupi et al. (2018), and Nickerson et al. (2019) maintain an SFR proportional to total gas density. Hu et al. (2016) find that SF correlates with H I-dominated cold gas better than with H_2 , and a significant presence of warm, non-star-forming H_2 gas. Lupi et al. (2018) argue that the KS law between H_2 and SFR arises naturally and their arbitrary link is unnecessary.

Properly modelling the gas chemistry is not only important to accurately compute gas cooling in numerical simulation but also to compute the H_2 abundance to compare with observed molecular KS law (Bigiel et al. 2008, 2010). This is particularly timely given the wealth of far-infrared data coming from recent (e.g. the *Herschel Space Observatory*; Pilbratt et al. 2010, low redshift) and current facilities such as the Atacama Large Millimeter/submillimeter Array (ALMA; ALMA-Partnership 2015). A more sophisticated treatment of these physical processes in numerical simulation will contribute to explore the nature of the relationship between SF and H_2 , to test SF recipes, and to describe the H_2 impact on the ISM characteristics.

In this work, we present a novel interface between an updated version of GADGET-3 (Springel 2005; Beck et al. 2016) and the chemistry package KROME (Grassi et al. 2014). We explicitly follow nine primordial (H, H_2 , He, and their ions) and seven metal species and model the corresponding non-equilibrium cooling using KROME.

An external radiation field is adopted following the scheme of Haardt & Madau (2012). Additionally, a stellar radiation feedback is modelled (Bruzual & Charlot 2003; Lupi et al. 2018; Plat et al. 2019). Chemical and energy feedback by Type II (SNII) and Type Ia (SNIa) Supernovae are followed within a multiphase ISM (Scannapieco et al. 2005, 2006). KROME has been consistently coupled to the latter scheme. With P-GADGET3-K, we explore different models of H_2 formation on dust and investigate the impact of metallicity in the H_2 networks and how it affects the properties of the H_2 distribution and the ISM. For this purpose, an initial condition (IC) corresponding to an idealized gas-rich Milky Way mass-size galaxy set to evolve passively is used. The initial chemical abundances follow a radial profile with a negative. We run this IC with different combination of parameters, dust model, SF algorithm, and metallicity dependence to explore the effects of H_2 production and identify which models and parameters better reproduce observations.

This paper is organized as follows. In Section 2, an overview of the adopted version of GADGET-3 and how KROME is grafting within it are provided. In Section 3, idealized simulations are analysed to test our method and compare the results with observations. Additionally, we test the robustness of our method against numerical resolution. Finally, in Section 4, we summarize our findings and provide future directions for our current work.

2 SIMULATION CODE

In this section, we describe P-GADGET3-K, which is the outcome of grafting the publicly available chemistry package KROME developed by Grassi et al. (2014), into the update implementation of GADGET-3 by Beck et al. (2016). Additionally, we discuss different implementations of the SF algorithm tested in P-GADGET3-K.

2.1 Main characteristics of the hydrodynamic code: GADGET-3

We use a version of GADGET-3 that incorporates the improved implementations of Beck et al. (2016) for the hydrodynamical evolution based on the smoothed hydrodynamical particle (SPH) technique. The density is estimated in a classic fashion from the mass distribution of gas particles weighted by the kernel function while the hydrodynamical forces are calculated according to the density-entropy formulation. However, instead of using the traditional cubic spline function, this version use the Wendland kernels (Dehnen & Aly 2012) with 200 neighbours, achieving better numerical convergence. As a result a more accurate density and density gradients estimations are obtained.

Additionally, the version of GADGET-3 used includes a high-order gradient computation from the full-velocity gradient matrix (Cullen & Dehnen 2010; Hu et al. 2014) and a shear flow limiter (Balsara 1995). It also implements a prescription for locally adaptive time-dependent artificial conduction (Price 2008; Tricco & Price 2013; Arth et al. 2019) to treat discontinuities in the internal energy (for purely numerical reasons), which corrects for gravitationally induced pressure gradients and improves the performance of the SPH scheme in capturing the development of gas-dynamical instabilities.

2.2 Chemical and energy feedback and the multiphase ISM model

Our current version, P-GADGET3-K, includes chemical and energy feedback by SNII and SNIa. For the energy SN feedback, the model of Scannapieco et al. (2006) is adopted. This model has been proven to successfully trigger galactic mass-loaded winds

without introducing mass-scale parameters or kicking gas particles, or suppressing the cooling in surrounding gas particles. The impact of galactic winds has been reported to naturally adapt to the potential well of the galaxy where SF takes place. A Salpeter initial mass function (IMF) is adopted (Salpeter 1955). The SN feedback is grafted within a multiphase model for the ISM described in detail by Scannapieco et al. (2005). This multiphase scheme allows the coexistence and material exchange between the hot, diffuse phase and the cold, dense gas phase. The thermodynamical and chemical changes are introduced on particle-by-particle basis, considering the physical characteristics of its surrounding gas medium (Marri & White 2003).

Briefly, in the SN feedback model, stars form in dense and cold gas clouds and part of them ends their lives as SNaE events, injecting energy, and chemical elements into the ISM. Both chemical elements and energy are distributed between the cold and hot phases of a given star particle (Scannapieco et al. 2008). We assume that 70 per cent of chemical material (Tissera et al. 2016b) and 50 per cent (Scannapieco et al. 2005) of the SN energy released are injected into the cold phase surrounding the stellar progenitor (the rest of the chemical elements and energy are injected into the surrounding hot phase). The released SN energy is thermalized instantaneously in the hot phase. Conversely, the cold phase stores the injected energy in a reservoir until there is enough energy to change the entropy of the cold gas particle so that it joins its hot phase. Hence, it is a self-regulated process and does not involve sudden changes in kinetic energy. The mass-loaded galactic winds induced by the SN model of Scannapieco et al. (2008) self-regulate according to the potential wells of the galaxies.

We use the chemical evolution model developed by Mosconi et al. (2001). This model considers the enrichment by SNII and SNIa adopting the elements yield prescriptions of chemical elements of Woosley & Weaver (1995) and Iwamoto et al. (1999), respectively. A set of 13 isotopes (H, ^4He , ^{12}C , ^{16}O , ^{24}Mg , ^{28}Si , ^{56}Fe , ^{14}N , ^{20}Ne , ^{32}S , ^{40}Ca , and ^{62}Zn) is followed in time. Galactic winds are responsible for transporting metals out of the galaxies from the cold ISM into the hot circumgalactic medium. Testing different values for the injection of chemical elements, Tissera et al. (2016b) found that the selected value provides a good description of the metallicity gradients of the stellar populations in the disc components of the galaxies when compared with the observational results from the CALIFA survey (Sánchez-Blázquez et al. 2014). The metallicity gradients of the gas-phase discs are also within the observed range (Tissera et al. 2016a).

The lifetimes for SNIa are randomly selected within the range [0.1, 1] Gyr. This model, albeit simple, is able to reproduce well mean chemical trends. Indeed, Jiménez, Tissera & Matteucci (2014, 2015), compared the median chemical abundances generated by this SNIa lifetime model and the Single Degenerated scenario for the delay time-life distribution (Matteucci & Recchi 2001), finding similar averaged trends (within the estimated dispersion).

This multiphase scheme improves the description of the thermodynamical characteristics of the regions where H_2 can be formed as it can better reproduce the cold and high-density regions, separated from the low-density ones. Without this model, the density and temperature (entropy) tend to have more homogeneous distributions towards higher and lower values, respectively (Marri & White 2003; Scannapieco et al. 2006). Hence, the areas where H_2 can be formed would not be well determined. In addition, chemical elements play a crucial role in determining the cooling rates and the dust-to-gas fractions. Having the enrichment of the baryons self-consistently described as the systems evolve (see Scannapieco et al. 2005, 2008) allows us to better simulate the evolution of the H_2 .

2.3 Main characteristics of the chemistry package KROME

The chemistry package KROME (Grassi et al. 2014) is a flexible PYTHON code that, given a set of chemical reactions, writes the necessary and optimized Fortran subroutines to solve the associated system of ordinary differential equations (ODEs) and follow the time-dependent evolution of the chemical species as well as the gas temperature. KROME employs the implicit high-order ODE solver ‘DLSODES’ (Hindmarsh 1983) to integrate this system and also provides a variety of models to describe several physical processes, including radiative and thermochemical cooling/heating, photochemistry, and dust physics. Finally, these subroutines can be embedded as a library in any hydrodynamics code. It has been successfully employed to study a variety of problems (environments and processes) as: black holes (Latif et al. 2019), SF activity (Lupi et al. 2018; Lupi & Bovino 2020), metal and molecular chemistry in galaxies and filaments (Bovino et al. 2016; Seifried et al. 2017; Capelo et al. 2018), first-stars (Latif & Schleicher 2015; Sharda, Krumholz & Federrath 2019), etc.

2.4 Modelling the gas chemistry and thermal processes

Chemistry and radiative cooling/heating are computed with KROME, following the model 1a described in Bovino et al. (2016). This model takes into account the photoheating, H₂ UV pumping, Compton cooling, photoelectric heating, atomic cooling, H₂ cooling, and chemical heating and cooling. Our own implementation includes the non-equilibrium rate equations for nine primordial species (i.e. H I, H II, H₂, H₂⁺, H⁻, He I, He II, He III, and e⁻) and also seven metal species (C I, C II, O I, O II, Si I, Si II, and Si III). In the latter case, a linear system for the individual metal excitation levels is solved on-the-fly for the most important coolants in the ISM (see Glover & Jappsen 2007; Maio et al. 2007).

In addition, following Lupi et al. (2018), we include three-body reactions involving H₂ (Glover & Abel 2008; Forrey 2013), H₂⁺ collisional dissociation by H, and H⁻ collisional detachment by He (Glover & Savin 2009). We clarify that these reactions are taken into account only for completeness, due to the very small reaction rate expected in the density range achieved in the simulations analysed in this work. H⁻ photodetachment is also incorporated, though its effect is expected to be relevant in low-metallicity regions. Our chemical network covers a total of 16 species and 70 selected reactions.

The dissociation of H₂ occurs via two main mechanisms, the excitation to the vibrational continuum of an excited electronic state and the Solomon process when dissociating and ionizing radiations are present (e.g. Bovino et al. 2016). To model this, we consider the contributions of ionizing fluxes from local stellar sources (see Section 2.6), and from a uniform extragalactic ultraviolet (UV) background adopting the model of Haardt & Madau (2012). Following Lupi et al. (2018), we define 10 energy bins, ranging from 0.75 to 1000 eV, to cover principally the characteristic energies for H⁻ photodetachment, H₂ and H₂⁺ dissociation, and the different hydrogen and helium ionization states (Katz et al. 2017).

The extragalactic background is unable to reach the innermost parts of a galaxy because of the shielding by the intervening gas and dust. To account for the attenuation of the radiation in these high-density regions, we assume that the UV background is diminished by a factor $\exp(-\tau)$, where $\tau_{\text{bin}} = \sum_i \sigma_{i, \text{bin}} N_i$ is the optical depth for every energy bin, $\sigma_{i, \text{bin}}$ is the cross-section in the bin for the *i*th species (pre-computed by KROME), and N_i is the *i*th species column density. We simplify this following Capelo et al. (2018) and assuming that the neighbouring gas surrounding each gas particle has similar

properties to the given particle. Then, the column density can be estimated as $N_i \sim n_i \lambda$, where n_i is the *i*th species number density and λ is the absorption length, which is assumed to be equal to the Jeans length L_J of a given gas particle. Safranek-Shrader et al. (2017) show that the Jeans length is a better approximation compared to gradient-based shielding lengths. Additionally, at high densities, gas clouds also self-shield from radiation. To consider this process and properly track the abundances in these regions without overestimating the effective radiative flux, self-shielding by H₂ and dust is adopted. Both terms are implemented in KROME as a sub-grid recipe following Richings et al. (2014b).

P-GADGET3-K includes the formation of H₂ by both possible channels: in gas-phase (e.g. reactions 7–8 and 9–10 in Bovino et al. 2016) and by catalysis on dust grains (Hollenbach & McKee 1979). The later channel dominates for high levels of metal enrichment ($Z \gtrsim 10^{-2} Z_{\odot}$) and dust-to-gas ratio.

2.4.1 H₂ formation on dust

The presence of dust is a critical aspect for the formation of H₂ in most of the relevant regions where SF can take place. We employ two models to describe this process:

(i) The scheme of Jura (1975, J75) that assumes fixed dust properties and no dependence on gas temperature, yielding the following rate

$$\frac{dn_{\text{H}_2}}{dt} = 3 \times 10^{-17} n_{\text{H I}} n_{\text{H}} \frac{Z}{Z_{\odot}} C_{\rho} \text{ cm}^{-3} \text{ s}^{-1}. \quad (1)$$

(ii) The model described by Tomassetti et al. (2014), following the precursors schemes of Tielens & Hollenbach (1985) and Cazaux & Spaans (2004), that adopts a dependence on the gas temperature resulting in a rate

$$\frac{dn_{\text{H}_2}}{dt} = 3.025 \times 10^{-17} n_{\text{H I}} n_{\text{H}} S_{\text{H}} \sqrt{\frac{T}{100 \text{ K}}} \frac{Z}{Z_{\odot}} C_{\rho} \text{ cm}^{-3} \text{ s}^{-1}, \quad (2)$$

where

$$S_{\text{H}} = \left[1 + 0.4 \left(\frac{T + T_{\text{d}}}{100 \text{ K}} \right)^{1/2} + 0.2 \frac{T}{100 \text{ K}} + 0.08 \left(\frac{T}{100 \text{ K}} \right)^2 \right]^{-1}$$

is the sticking probability coefficient of the H atoms, which depends on gas and dust temperatures. For simplicity, here we adopt a constant dust temperature $T_{\text{d}} = 10$ K, value typical of molecular clouds, following the works of Tomassetti et al. (2014), Richings et al. (2014a), and Bovino et al. (2016). These last two articles showed that, in the range of gas densities considered in their simulations, similar in resolution to our experiments, T_{d} is not strongly affected by the interaction between dust and gas, and therefore, the approach where T_{d} is calculated by solving the thermal equilibrium equation produces equivalent results to that where T_{d} is kept constant.

In these models, we do not compute the dust temperature or the gas cooling by dust. However, its impact is not relevant in the density range $n_{\text{g}} \lesssim 10^7 \text{ cm}^{-3}$ (see Bovino et al. 2016; Grassi et al. 2017). This density threshold is larger than the maximum density reached in our simulations.

For both models $n_{\text{H}} = n_{\text{H I}} + n_{\text{H II}} + n_{\text{H}^-} + 2n_{\text{H}_2} + 2n_{\text{H}_2^+}$ is the total H number density, and we assume that the mass dust-to-gas ratio, $D \equiv \rho_{\text{d}}/\rho_{\text{g}}$, scales linearly with metallicity as $D = D_{\odot} Z/Z_{\odot}$, where $D_{\odot} = 0.00934$ (Yamasawa et al. 2011). However, we note that Aoyama et al. (2017) claim that, at high redshift ($z \gtrsim 3.5$), this

correlation breakdown. This change might be important to test in cosmological simulations.

C_ρ is a clumping factor that takes into account the possible missed H_2 formation in the high-density regions due to limited numerical resolution. In the next section, we will explore the impact of the clumping factor by running the same IC with $C_\rho = 1$ (i.e. no clumping factor), 10 and 100. We will also explore a variable clumping factor following Lupi et al. (2018):

$$C_\rho = 1 + b^2 \mathcal{M}^2, \quad (3)$$

where \mathcal{M} is the Mach number, and b a turbulent parameter that describes the ratio between compressive and solenoidal turbulence and its typical value is $b = 0.4$, for a statistical mixture of these turbulences (Federrath et al. 2010).

2.4.2 Thermal processes

The thermal behaviour (cooling/heating) of the gas is an extremely important physical process that has profound effects on the evolution of a galaxy, since it has direct impact on the SF, among other phenomena. In this work, we include via KROME the following thermal processes: H I, He I, and He II collisional excitation and ionization, H II, He II, and He III recombination, He I dielectronic recombination, Compton cooling from the CMB-relevant for cosmological simulations, bremsstrahlung (Cen 1992), H_2 roto-vibrational cooling (Glover & Abel 2008; Glover 2015; Bovino et al. 2016) and collisional dissociation (Omukai 2000), dust surface recombination (Bakes & Tielens 1994), and metal-line cooling [see e.g. Grassi et al. (2014) and Bovino et al. (2016) for a thorough explanation].

Metal-line cooling is a dominant process for gas with relatively high metallicity and low density. However, at high temperatures, given the large number of metal species, their ionization states, transitions, and collisional processes, it becomes computationally expensive to properly follow the detailed metal network and its related non-equilibrium cooling. Moreover, for $T \gtrsim 10^4$ K, it is reasonable to assume thermochemical equilibrium and employ photoionization equilibrium (PIE) metal cooling tables, due to the presence of a radiation background. Therefore, for $T \gtrsim 10^4$ K, we adopt the PIE table computed by Shen et al. (2013) using Cloudy (Ferland et al. 1998) and considering an extragalactic radiation background by Haardt & Madau (2012). This table provides the metal cooling rates as a function of gas temperature ($10 \leq T \leq 10^9$ K), density ($10^{-9} \leq n_H \leq 10^4 \text{ cm}^{-3}$), and redshift ($0 \leq z \leq 15.1$). Moreover, these rates are provided assuming solar abundances and then linearly re-scaled with the metallicity Z of each particle, which is followed as a passive scalar.

On the other hand, for a gas temperature $T < 10^4$ K, where the assumption of equilibrium does not hold, we use the non-equilibrium cooling rates by C I, C II, O I, O II, Si I, and Si II because these elements are the most important metal coolants in the ISM (see Wolfire et al. 2003; Shen, Wadsley & Stinson 2010; Richings et al. 2014a). In this case, KROME solves an equilibrium linear system using on-the-fly coolant and collider(s) abundances and temperature for the individual excitation levels of these metal atoms and ions.

2.5 Star formation scheme

The processes involved in the transformation of gas into stars are complex and act on smaller scales than those involved in the galaxy assembly. To model these phenomena, SF sub-grid recipes are used. SF algorithms usually adopt thresholds to define the dense and cold

gas that is in condition to be transformed into stars following a probabilistic approach (Springel & Hernquist 2003). The new star particles, which are assumed to represent simple stellar populations, are stochastically created according to the probability derived from the SFR of each gas particle. The likelihood for a gas particle to be transformed into stars is computed using different schemes. In this paper, we consider two methods.

On one hand, the ‘classic’ recipe assumes that a gas particle with temperature $T < T_{\text{SF}} = 10^3$ K and density $\rho_g > \rho_{\text{SF}} = 8 m_H \text{ cm}^{-3}$, is in condition to form a star particle according to

$$p_1 = (m_g/m_s) \left[1 - e^{-(\epsilon_* dt/t_{\text{dyn}})} \right], \quad (4)$$

where m_g , dt , and $t_{\text{dyn}} = \sqrt{3\pi/(32G\rho)}$ are the mass, time-step, and dynamical time of each star-forming gas particle, and G is the gravitational constant. m_s will be the stellar mass created (a preset fraction f_s of the gas particle mass) and ϵ_* is the SF efficiency parameter (Springel & Hernquist 2003; Krumholz & McKee 2005).

On the other hand, following Hopkins et al. (2018), the second method selects a gas particle to form stars based on the so-called virial parameter α , which restricts the formation of stars only to self-gravitational regions, i.e. those particles that are prone to gravitational collapse (Semenov, Kravtsov & Gnedin 2016):

$$\alpha_i = \frac{\|\nabla \otimes \mathbf{v}_i\|^2 + (c_{s,i}/\delta r_i)^2}{8\pi G \rho_i}. \quad (5)$$

This ‘self-gravity’ method allows only gas particles with $\alpha < 1$ to be transformed into stars, which indicates that these gas particles cannot overcome gravitational collapse through kinetic or thermal support. Here, \mathbf{v}_i is the gas velocity, $c_{s,i}$ the sound speed, δr_i the particle size and $\|\nabla \otimes \mathbf{v}_i\|^2$ is the Frobenius norm of the velocity dispersion matrix, defined as

$$\|\nabla \otimes \mathbf{v}_i\|^2 = \sum_{i,j} \left(\frac{\partial v_i}{\partial x_j} \right)^2. \quad (6)$$

We also incorporated a simple H_2 -dependent SF algorithm that uses the fraction of molecular hydrogen f_{H_2} per gas particle to weight the probability according to

$$p_2 = \begin{cases} p_1 f_{H_2} & Z/Z_\odot > 10^{-3} \\ p_1 (1 - \alpha) & Z/Z_\odot \leq 10^{-3}. \end{cases} \quad (7)$$

The lower metallicity threshold adopted to weight by the H_2 fraction is imposed considering that in the case of pristine gas $f_{H_2} \sim 0$ and hence, no SF would occur. Previous theoretical works (e.g. Maio et al. 2010) and observations of very metal poor stars (e.g. Frebel et al. 2010) suggest that at the metallicity (Z_{crit}) at which the metal cooling function dominates over the molecular one, the modalities of SF transition from Population III SF regime to the standard Population II-I regime. Different studies suggest Z_{crit} varies from $\sim 10^{-6} Z_\odot$ (Schneider et al. 2006) to $\sim 10^{-3} Z_\odot$ (Bromm & Loeb 2003; Bovino et al. 2014). For this analysis, we adopt the latter as our metallicity threshold.

Both probability functions, p_1 and p_2 , imply that, on average, $dM_*/dt = \epsilon_* m_g/t_{\text{dyn}}$, effectively ensuring that SF follows the slope of the KS law (Schmidt et al. 1959; Schmidt 1963; Kennicutt 1989, 1998) between SFR and gas surface densities, whereas the normalization can be matched by tuning the SF efficiency parameter, ϵ_* . We run our simulations with $\epsilon_* = 0.01$ (Krumholz, Dekel & McKee 2012). With this value the normalization of the KS law is fairly well-reproduced and is consistent with the average SF efficiency computed as a function of the gravo-turbulent state of the gas in Lupi et al. (2018).

2.6 Stellar radiation scheme

In addition to the extragalactic UV background, we also include a phenomenological model to take into account the radiation field from the nearby stellar populations. Due to the strong ionizing and dissociating flux produced principally by young stars, this form of radiative feedback has a significant impact on the H_2 abundance. To estimate the contribution of the young stellar populations, we assume that every star particle generated in our simulations forms in an instantaneous SF burst, which produces a simple stellar population. A Salpeter IMF, with lower and upper mass cutoffs of $m_L = 0.1 M_\odot$ and $m_U = 100 M_\odot$, is adopted to estimate the number of stars of a given stellar mass. Then, we use the Salpeter IMF version of the C&B SSP models described in Plat et al. (2019) to follow the age and metallicity dependent spectral evolution of the luminosity L_* of each star particle. The C&B models are an updated version of the Bruzual & Charlot (2003) models, which incorporate, most notably, a new prescription for the evolution of massive stars from Chen et al. (2015) and higher resolution spectral libraries (see Plat et al. 2019 for details).

To calculate the total flux that radiates to a gas particle, different models have been proposed. Christensen et al. (2012) calculate the average flow of nearby stars using the tree structure employed for gravity computation. Similarly, Hopkins et al. (2014, 2018) and Lupi et al. (2018) use the total luminosity and the luminosity-weighted centre of the stellar sources within each tree node. However, efficient H_2 and dust shielding at high densities makes the H_2 fraction relatively insensitive to the amount of dissociation radiation incident on molecular clouds (Gnedin, Tassis & Kravtsov 2009; Krumholz, McKee & Tumlinson 2009; Mac Low & Glover 2012). To consider this attenuation and shielding, Christensen et al. (2012) assume that the column length is equal to the smoothing length h of the target gas particle. However, this scheme may be susceptible to resolution effects. In this regard, Safranek-Shrader et al. (2017) evaluate several common approximations for the shield length, such as the Sobolev approximation, the Jeans length, a single cell and power-law approximations, and a length based on the local density and its gradient. They compare these implementations to a detailed ray-tracing solution for the radiative transfer problem and find that a temperature-limited Jeans length work well to equal effective visual extinction and performs better than other local models in calculating the weighted mass abundances of H_2 and CO. Byrne et al. (2019) reinforce these conclusions.

Based on these results, we opt for a model that loops over gas particles gathering all star particles within a maximum distance R_c , assumed to be equal to the Jeans length of the target gas particles

$$L_{J(T < 40\text{K})} = \sqrt{\frac{\pi c_s^2}{G\rho}} = \sqrt{\frac{\pi}{G\rho} \frac{\gamma T k_B}{\mu m_H}}, \quad (8)$$

where T is the gas temperature with a ceiling value of 40 K, γ and μ , the adiabatic coefficient and the mean molecular weight of gas, respectively, and k_B , the Boltzmann constant. This choice is consistent with the attenuation model adopted by KROME. We also impose the condition $R_c = \max(R_c, 5h)$ since a factor of 5 represents a good compromise between collecting radiation from large enough distances and restricting the computational overhead (Lupi et al. 2018).¹

¹This upper limit, $R_c = 5h$, is seldom reached, except for gas particles in extreme low-density regions.

Hence, considering all stellar particles within R_c , we compute the total radiative flux, in each of 10 defined energy bins (ranging from 0.75 to 1000 eV, see Section 2.4), which reaches a target gas particle as

$$F = \sum_j \left(\frac{L_{*,j}}{4\pi d_j^2} \exp(-\tau_j) \right), \quad (9)$$

where $L_{*,j}$ and d_j are the luminosity and the distance to the j th stellar particle, respectively. Since we cannot estimate the real optical depth τ_j of the total gas located between the different stellar sources and the target gas particle, for each energy bin, τ_j is approximated by using its species abundances and an absorption length equal to d_j ($\tau_{j,\text{bin}} \approx \sum_i \sigma_{i,\text{bin}} n_i d_j$).

Additionally, we consider the attenuation from dust computed from the dust-to-gas ratio dependent scheme ‘Milky Way, $R_V = 3.1$ ’ by Weingartner & Draine (2001). This is a carbonaceous-silicate grain model with a Milky Way-size distribution for $R_V^2 = 3.1$. This value successfully reproduces observed interstellar extinction, scattering, and infrared emission, and is considered to be appropriate for typical diffuse H I clouds in the Milky Way (Draine 2003).

2.7 Initial conditions

We perform different simulations of the same IC representing an isolated galaxy to test the main parameters associated with KROME and the models for the dust and SFR implementations in our code as summarized in Table 1.

The IC we adopted for the tests (hereafter, standard IC) corresponds to a disc galaxy formed by a dark matter halo of $9 \times 10^{11} M_\odot$, a bulge of $1.30 \times 10^{10} M_\odot$, and a disc component of $3.90 \times 10^{10} M_\odot$. We assume that 50 per cent of disc mass is in the gas phase. The standard IC allows us to test different parameters faster. A higher resolution version is used to test convergence.

For the standard IC, the galaxy components are resolved by 2×10^5 dark matter particles of $4.5 \times 10^6 M_\odot$, 6×10^4 and 4×10^4 star particles of $3.25 \times 10^5 M_\odot$, in the disc and bulge components, respectively, and initially 10^5 gas particles of $1.95 \times 10^5 M_\odot$. The initial dark matter profile is consistent with an NFW profile (Navarro, Frenk & White 1996) with a virial circular velocity of 160 kms^{-1} . The disc component follows an exponential profile with a scale-length of 3.46 kpc while the bulge follows a Hernquist profile. The gravitational softenings adopted are 0.32, 0.20, and 0.16 kpc, for the dark matter, star, and gas particles, respectively.

An important aspect to take into account is that the spatial initial metallicity distribution of the gaseous disc in our standard IC has been set to have an initial radial profile with a gradient of $\nabla_{(O/H)} = -0.1$ dex kpc^{-1} and the central abundance, $(O/H)_c = 12 + \log(O/H) = 8.5$. The later is determined so that the IC is consistent with the mass-metallicity relation at $z \sim 2$ (Maiolino et al. 2008). Additionally, for consistency, we choose the model of Haardt & Madau (2012) for a uniform extragalactic UV background at the same redshift ($z = 2$). With this characteristic, the IC represents a massive gas-rich galaxy that evolves transforming its gas reservoir in isolation since $z \sim 2$. Although it is an idealized IC, it allows the exploration of the H_2 fraction and SF activity evolution using different model prescriptions.

In Section 3.5, the effects of numerical resolution will be evaluated. For this purpose, we run a high resolution IC which adopt the same characteristics of the standard IC but increasing the number

² $R_V \equiv A(V)/E(B - V)$ is the ratio of visual extinction to reddening.

Table 1. Main parameters of simulations: (1) Run name. (2) Model of H_2 formation on dust. (3) Clumping factor: fixed or variable. (4) SF recipe. (5) Metal cooling model for the gas at low temperatures $T < 10^4$ K. (6) Gas metallicity: fixed values without further enrichment by any source, and initial primordial gas (Z_p) or an initial metallicity gradient corresponding to $z \sim 2$ [(Maiolino et al. 2008) – Z_g]. In the latter two cases, chemical evolution is fully included (see Section 2). (7) Stellar radiation feedback.

Run ⁽¹⁾	H_2 -dust model ⁽²⁾	C_ρ ⁽³⁾	SF recipe ⁽⁴⁾	Metal cooling ⁽⁵⁾	Z ⁽⁶⁾	Stellar Rad ⁽⁷⁾
c1	J75	1	Thresholds	Non-equilibrium	Z_g	No
c10	J75	10	Thresholds	Non-equilibrium	Z_g	No
c100	J75	100	Thresholds	Non-equilibrium	Z_g	No
cv	J75	Var	Thresholds	Non-equilibrium	Z_g	No
c100T	T14	100	Thresholds	Non-equilibrium	Z_g	No
S	J75	100	Self-grav	Non-equilibrium	Z_g	No
SH2	J75	100	Self-grav and f_{H_2}	Non-equilibrium	Z_g	No
SH2_SR	J75	100	Self-grav and f_{H_2}	Non-equilibrium	Z_g	Yes
eZ	J75	100	Self-grav and f_{H_2}	Equilibrium	Z_g	No
eZ01	J75	100	Self-grav and f_{H_2}	Equilibrium	$0.1 Z_\odot$	No
eZ05	J75	100	Self-grav and f_{H_2}	Equilibrium	$0.5 Z_\odot$	No
LR	J75	100	Self-grav and f_{H_2}	Non-equilibrium	Z_p	No
HR	J75	10	Self-grav and f_{H_2}	Non-equilibrium	Z_p	No

of particles per galaxy component: 10^6 dark matter particles (mass of $9 \times 10^5 M_\odot$), 10^5 star particles (mass of $1.3 \times 10^5 M_\odot$) in the bulge, and 4×10^5 (mass of $4.8 \times 10^4 M_\odot$) in the disc. In addition, 10^6 initial gas particles (initial mass of $1.9 \times 10^4 M_\odot$) are available. The respective gravitational softenings for all components are 0.2, 0.15, 0.1, and 0.08 kpc, respectively. For this case, the initial chemical content of the gas is pristine, that is, it is initially composed of H and He only, without the imposition of any metallicity gradient (as done in some previous works). A lower resolution counterpart (with pristine gas) has been also performed in order to properly assess the impact of numerical resolution under similar conditions.

3 RESULTS

In this section, we focus on assessing the impact of the clumping factor and the models of H_2 formation on dust (hereafter H_2 -dust models in this text). For this purpose, we analyse the distributions of H_2 and H I and the implications of numerical resolution. In addition, we explore the metal-dependence of the H_2 content and its impact on the SF activity and the KS law. The analysis is performed at $t \sim 0.6$ Gyr of evolution of the systems when the main starburst has ended, but the system is still actively forming stars (SFR $\sim 8 M_\odot \text{ yr}^{-1}$). We stack the analysed quantities over a period of $0.4 \leq t \leq 0.8$ Gyr, to provide overall estimations that are more stable against possible sharp variations due to numerical resolutions.

3.1 Genesis of H_2 on dust: the formation models and clumping factor

In this section, we analyse the J75 H_2 -dust scheme, for different clumping factors, $C_\rho = 1, 10, 100$ and a variable C_ρ (cv). Additionally, we perform a run with T14 H_2 -dust model and $C_\rho = 100$ for comparison.

First, we focus on J75 H_2 -dust scheme, for different clumping factors, $C_\rho = 1, 10, 100$. In Fig. 1, we show the face-on and edge-on projected gas density maps coloured by the mass-weighted

temperature³ (first column) and the projected surface distributions of SFR (Σ_{SFR} ; second column), H_2 (Σ_{H_2} ; third column), and H I ($\Sigma_{H\text{I}}$; fourth column) surface densities, for runs with the J75 H_2 -dust model and different constant C_ρ . Because the rate of H_2 synthesis in dust surface is directly proportional to the clumping factor, as it increases, the molecular content in the central regions grows while it extends to higher galactocentric distance and lower gas densities for higher C_ρ .

Otherwise, the spiral arm patterns in the face-on projection are very similar in all runs, suggesting that the effect on the global dynamics is not very relevant. None the less, most of H_2 still resides in the dense regions of the galaxy spiral arms, where the gas is expected to be cold and turbulent. The H I distributions are more homogeneous as expected. However, for smaller C_ρ they are concentrated preferentially in gas clumps located in the densest regions. As the clumping factor increases, we observe that the gas clumps, due to favourable high densities and low temperatures, begin to be dominated by the molecular content catalysed by dust and therefore the H I surface density decreases whereas the H_2 abundance gets more prominent. However, these differences in H_2 abundance do not have a large effect on the gas density–temperature configuration because, in the densities and metallicities considered in these simulations, molecular cooling has an average impact lower than metal cooling.⁴

In the bottom row of Fig. 1, we show the same distributions but assuming a variable clumping factor (Section 2.4, equation 3). For the SFR density and associated molecular clumps, their distributions are clumpier because large values of C_ρ (Lupi et al. 2018) are generated in dense, cold gas regions compare to C_ρ values outside them. This is due to its quadratic dependence on the velocity field (see Section 2.4)

³The face-on and edge-on temperature maps are constructed by weighted the temperature by the gas mass particle located in projected bins of $\sim 2 \times \epsilon_g$ length size.

⁴We note that the numerical resolution of these simulations is not high enough to follow the chemistry of CO, and therefore the cooling processes considered do not include this molecule. However, in reality, the synthesis of H_2 would be followed by the formation of CO, and cooling by CO rotational levels would further reduce the temperature from ~ 100 K down.

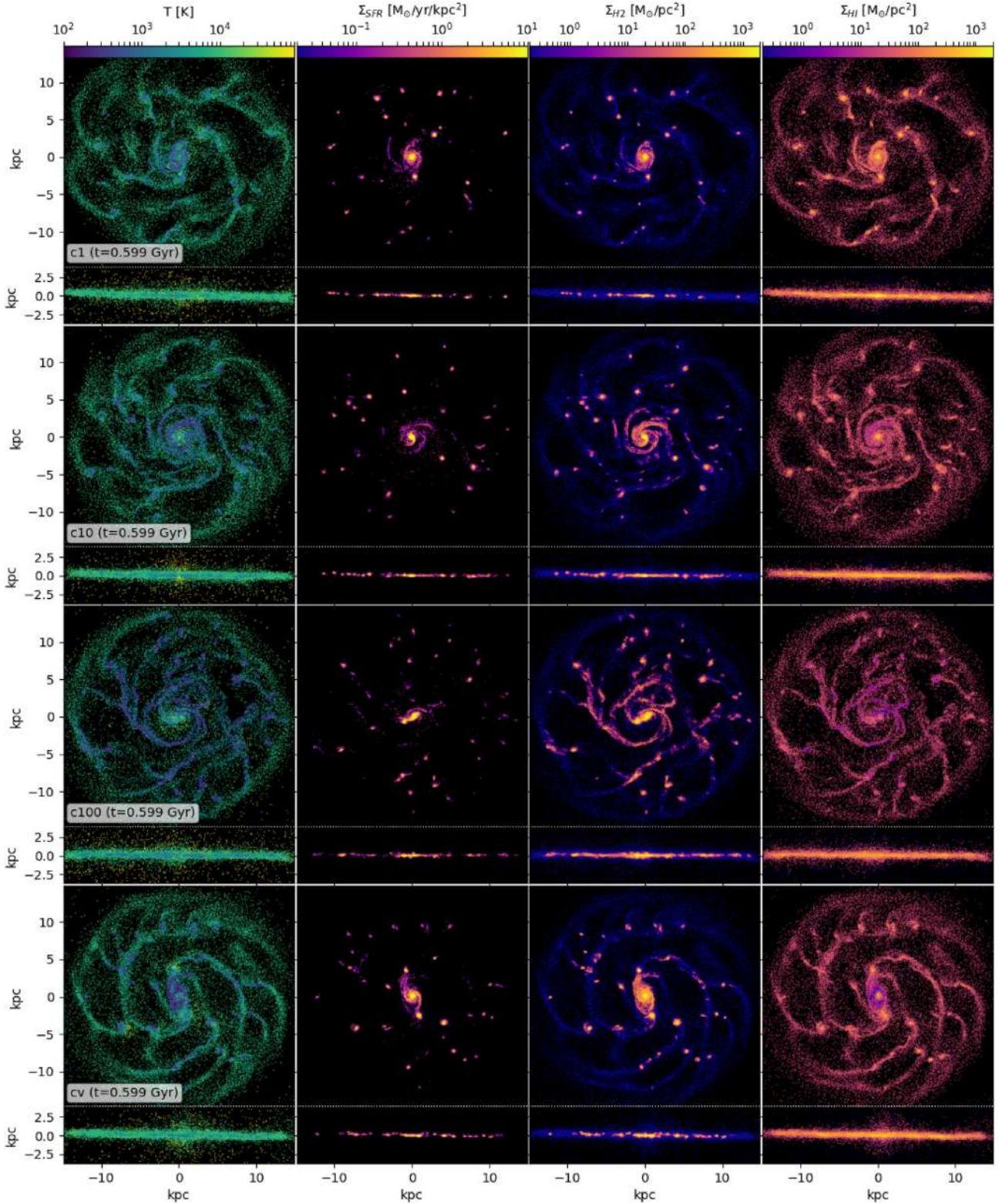


Figure 1. Face-on and edge-on maps (small panels) of the mass-weighted gas temperature (first column) and the projected surface density of SFR (second column), H_2 (third column), and $H\text{I}$ (fourth) content in c1 (first row), c10 (second row), c100 (third row), and cv (fourth row) runs of our idealized spiral galaxy.

that strongly favours supersonic turbulent motions, characteristic of the above clouds (Larson 1981).

To assess the effects of varying the dust model in Fig. 2, we show the face-on and face-edge distributions for the run with T14 H_2 -

dust models, which includes a dependence on the gas temperature and a fixed $C_p = 100$. As can be seen, the gas distributions are slightly smoother compared to previous, with less defined spiral patterns. In addition, the high-density regions of the spiral arms

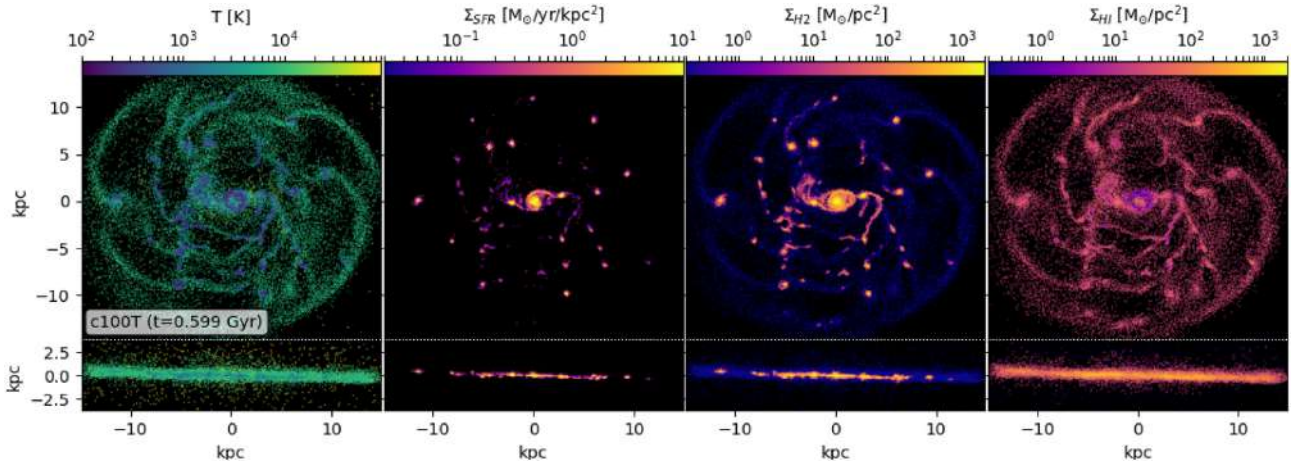


Figure 2. Face-on and edge-on maps for c100T simulations as shown in Fig. 1.

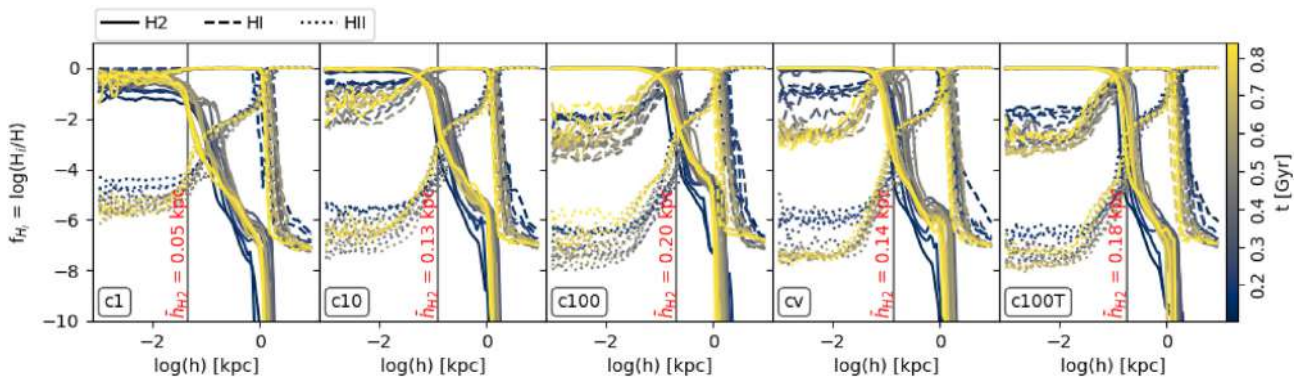


Figure 3. Vertical distribution of the fractions of H_2 (solid lines), $H\text{I}$ (dashed lines) and $H\text{II}$ (dotted lines) for simulations c1, c10, c100, cv, c100T. The vertical lines denote the average h_{H_2} , the perpendicular distance from the middle plane of galaxy, where $f_{H_2} = 0.1$. We define the thickness of molecular discs as $2h_{H_2}$.

exhibit a more vigorous H_2 formation with a more clumping distribution.

In the edge-on view (small panels in Figs 1 and 2), we can see that runs with larger clumping factor exhibit thicker molecular discs. This can be clearly appreciated in Fig. 3, where the vertical distributions of H_2 , $H\text{I}$, and $H\text{II}$ fractions are shown. The fraction $f_{H_i} = M_{H_i}/M_H$ is generically defined for each particle as the ratio between the mass of a species i of hydrogen and the mass of the total hydrogen content. With this information, we define the thickness of the molecular discs as $2 \times h_{H_2}$, where h_{H_2} is the height from the rotation plane of the galaxy at which $f_{H_2} = 0.1$. For $f_{H_2} < 0.1$, we assume the discs are dominated by $H\text{I}$ (Leroy et al. 2008). As shown in Fig. 3, we find that the average disc thickness effectively grows as C_ρ takes higher values, from $h_{\text{disc}} \sim 100$ pc for c1, $h_{\text{disc}} \sim 260$ pc for c10, and $h_{\text{disc}} \sim 400$ pc for c100. We also see that in all cases the molecular disc becomes slightly thinner as the system evolves. Adopting a variable clumping factor yields $h_{\text{disc}} \sim 140$ pc similar to c10, because the median of C_ρ distribution is $\sim 13 \pm 4$ with 25 and 75 percentiles at $C_\rho = 25$ and 65, respectively. These values are in very good agreement with those reported by Capelo et al. (2018).

After a first qualitative comparison, we now quantitatively assess the differences amongst the models. The amount of H_2 varies significantly when we vary the clumping factor and/or the H_2 -dust scheme (since it is the main formation channel for our initial conditions). Fig. 4 shows the phase diagrams of H_2 mass fraction versus n_H (cm^{-3}) per gas particle, of runs c1, c10 and c100, cv

and c100T. Additionally, the dotted lines indicate the percentiles 25, 50, and 75 of each H_2 fraction distribution. As expected, a larger clumping factor increases the amount of H_2 per gas particle. For c1 run ($C_\rho = 1$) just over 25 per cent of gas mass has an $f_{H_2} > 0.25$ while for c10 run ($C_\rho = 10$), 45 per cent of gas mass has this molecular fraction, and the 25 per cent exhibits an $f_{H_2} > 0.9$. In the case of the run c100 ($C_\rho = 100$), the 50 per cent of gas mass has a molecular fraction of $f_{H_2} > 0.75$ and the 25 per cent display an $f_{H_2} > 0.95$. With the same previous clumping factor, the T14 model (c100T) has the 50 per cent of gas particles with $f_{H_2} > 0.52$ and the 25 per cent, with $f_{H_2} > 0.95$.

Then, the selection of the model for H_2 formation on dust is relevant, but the choice of C_ρ is more significant at least for this numerical resolution. These results are in agreement to those reported by Capelo et al. (2018), where the impact of varying C_ρ in the J75 scheme and in the model of Cazaux & Spaans (2009) is analysed. As they argued, this is because their simulations, and ours, involve relatively high metallicity where the behaviour of H_2 -dust schemes are similar. This key aspect is well reflected in the cv run (J75 scheme with variable C_ρ) where the 25 per cent of gas particles have an $f_{H_2} > 0.95$ similar to run c100, but 50 per cent of them have an $f_{H_2} < 0.1$ as in run c10. Additionally, in Section 3.4 we will discuss the effects of metallicity on the H_2 production and cooling.

In all runs, the transition from the neutral to the fully molecular phase occurs between $n_H \sim 1$ and $\sim 100 \text{ cm}^{-3}$, in agreement with

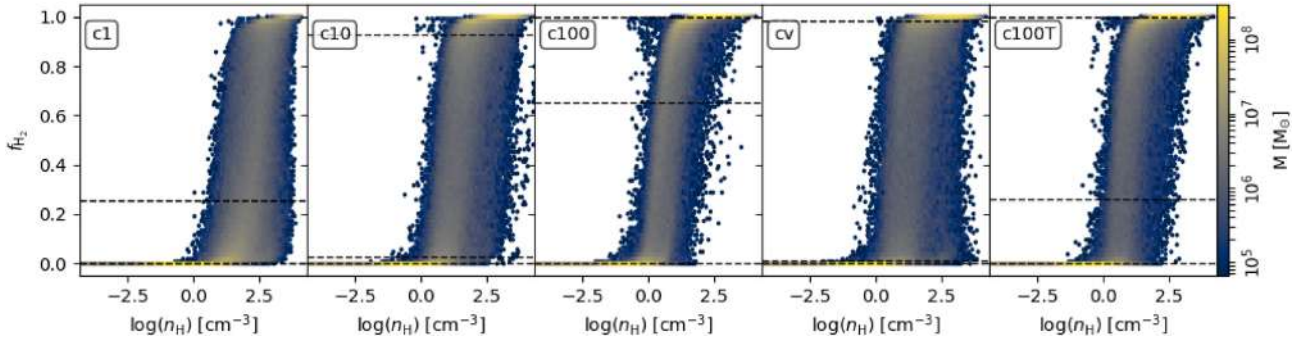


Figure 4. Phase diagrams of H_2 mass fraction versus n_{H} per particle, for runs with c1, c10, c100, cv (a variable C_{ρ}), and c100T. The horizontal dashed lines indicate the 25, 50, and 75 percentiles of the distributions of H_2 fractions. In the leftmost panel, the 50 and 75 percentiles are very close to values of $f_{\text{H}_2} < 10^{-2}$.

previous works (e.g. Gnedin et al. 2009; Christensen et al. 2012), where the gas becomes fully molecular above $n_{\text{H}} \sim 100 \text{ cm}^{-3}$. However, the transition region becomes thinner and moves at lower densities as the clumping factor increases for J75 model. Conversely, a variable clumping factor produces a wider transition zone because of its dependence on dynamical properties of the gas particles. Note that the density estimation in simulations is limited by numerical resolution, which is why this factor is incorporated into the models. Nevertheless, it has been shown that for higher numerical resolution, clumping factors are not required (Nickerson et al. 2019). The impact of resolution will be discussed in Section 3.5

We now compare the H_2 column density with local observations (Lupi et al. 2018). For this purpose, we compute the column density of both atomic (N_{H}) and molecular (N_{H_2}) hydrogen, in a square grid with cells of 1-kpc size, projected on to the galactic plane. In Fig. 5, N_{H_2} as a function of the total column density, defined as $N_{\text{H}_2} + N_{\text{H}}$, is displayed for c1, c10, c100, c100T, and cv experiments. The results are binned in 100 log-spaced bins along both axes. The colour code represents the number of cells in each bin. Observational results are included for comparison, where measurements from absorption spectra of distant AGNs and nearby stars are taken primarily from the Copernicus and FUSE surveys for the Milky Way (MW) and the Large and Small Magellanic Clouds (LMC and SMC). We consider the data by Tumlinson (2002) for the LMC and SMC, with $\bar{Z}_{\text{LMC}} \sim 0.4$ and $\bar{Z}_{\text{SMC}} \sim 0.1 Z_{\odot}$, respectively. For the MW ($\bar{Z}_{\text{MW}} \sim Z_{\odot}$), the data for the disc (Shull et al. 2021) and the halo (Gillmon et al. 2006) are depicted. Also we include the recompiled data by Wolfire et al. (2008).

Additionally, in Fig. 6 we compare the projected H_2 -to- H I surface density ratio, $R_{\text{mol}} = \Sigma_{\text{H}_2} / \Sigma_{\text{H I}}$, with the observational data of 23 nearby disc galaxies from the HERACLES survey collected by Leroy et al. (2008). These authors estimate different quantities for 23 nearby star-forming galaxies (of which 12 are large spiral galaxies). Their radial profiles are obtained within $1.2r_{25}^5$ using the means for $\Sigma_{\text{H I}}$, Σ_{H_2} , Σ_{SFR} , and the median Σ_{*} within 10 arcsec wide rings inclined. Since the average distance of this spiral galaxy subsample is ~ 8.5 Mpc, the mean width of the ring is ~ 400 pc ($10 \text{ arcsec} \sim 4.8 \times 10^{-5}$). Hence, we use the same value for our radial binning within $1.2r_{83}^6$. For these galaxies, Leroy et al. (2008) found that the

⁵The isophotal radius corresponding to 25 B -band magnitudes per square arcsec.

⁶ r_{83} is the radius that encloses 83 per cent of the luminous mass. For an exponential disc (Freeman 1970), r_{83} corresponds to the de Vaucouleurs 25 B -mag arcsec $^{-2}$ photometric radius. For the simulations we assume $M/L = 1$

transition between an H I and H_2 -dominated ISM ($R_{\text{mol}} = 1$) is a well-determined function of locally defined quantities in the galaxy that occur at characteristic values for most of the parameters considered, such as the gas (Σ_{gas}) and star (Σ_{*}) surface density. Also, they found that when the ISM is mostly H_2 -dominated in the inner parts of discs of spiral galaxies, the SF efficiency (SFE, defined as the ratio of the star formation rate to the gas mass of a parent cloud) is roughly constant as a function of the mentioned parameters ($\text{SFE}(\text{H}_2) = 5.25 \pm 2.5 \times 10^{10} \text{ yr}^{-1}$; see Section 3.3).

However, when the ISM is H I -dominated, the SFE declines steadily with increasing radius or other quantities covariant with it, as Σ_{*} , pressure or orbital time. They concluded that this implies that, while SF within GMCs is largely decoupled from environment, the synthesis of H_2 from H I , and by extension, the cloud formation, sensitively depends on local conditions. Thus, the behaviour of the SFE can be explained through two processes, the SF within GMCs and the formation of GMC itself. Then, the formation efficiency would prove to be the product of a constant SFE from H_2 and R_{mol} , which is a function of local conditions.

In Fig. 6, red contours enclose the 50 per cent (dash-dotted) and 95 per cent (solid) of direct measurements of R_{mol} from CO and H I assembled following the methodology used by Blitz & Rosolowsky (2006), while the cyan contours contain the inferred R_{mol} from Σ_{SFR} . Here, because of the limited sensitivity of the CO data, these direct measurements of R_{mol} seldom probe far below 1. Therefore, Leroy et al. (2008), assuming a fixed $\text{SFE}(\text{H}_2)$ for different concentric tilted rings, convert Σ_{SFR} into Σ_{H_2} and then divide this by the observed $\Sigma_{\text{H I}}$ to compute R_{mol} for that ring. In addition, the continuous lines show the fits found by Leroy et al. (2008), the horizontal dashed lines denote $R_{\text{mol}} = 1$ ($\Sigma_{\text{H I}} = \Sigma_{\text{H}_2}$) and the vertical dashed lines show the observational estimations of Σ_{*} and r/r_{83} at the H I -to- H_2 transition (the 1σ uncertainties of these estimates are denoted by the vertical dotted lines).

As can be seen from this figure, the agreement between direct measurements of R_{mol} and the simulation estimates is quite good. R_{mol} is a continuous function of environment spanning from the H_2 -dominated (~ 10) to H I -dominated (~ 0.1) ISM, from inner to outer galaxy discs, and over a wide range of ISM pressures.

All our models generate relations within the observational range. In particular, the runs with $C_{\rho} = 100$ show the best fits to observational distributions as a function of stellar mass density and radius remarkably well, independently of the dust-formation model. The model with a variable C_{ρ} (cv) exhibits a larger dispersion than c100 or c100T distributions and, on average, underestimates the observed measurements. However, as emphasized by Lupi et al. (2018), who

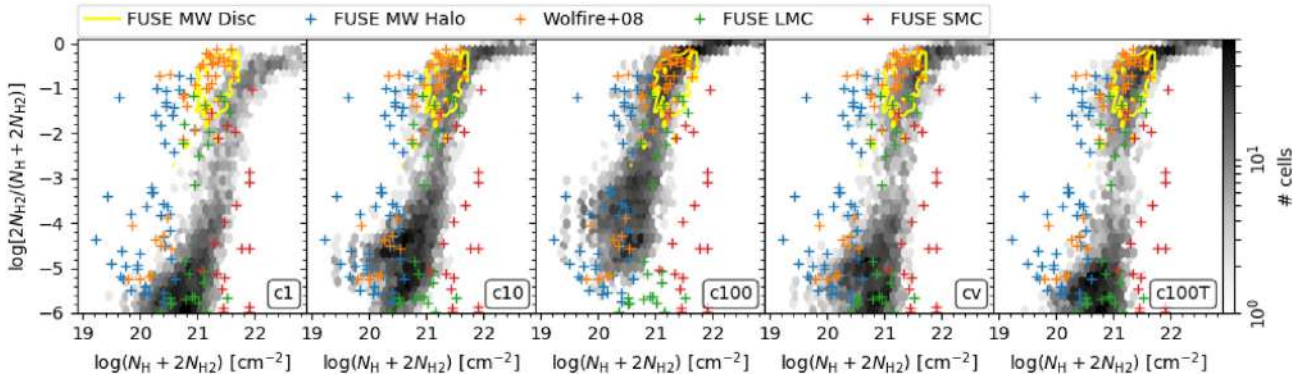


Figure 5. H_2 column density fractions, computed in a square grid projected on to the galactic plane, for the runs in Fig. 4, compared to observations of molecular clouds in the LMC, SMC (Tumlinson 2002 – green, red cross) and MW (disc data from Shull, Danforth & Anderson 2021 – yellow contour enclose all of them; halo data from Gillmon et al. 2006 – blue cross; recompiled data by Wolfire et al. 2008 – orange cross). The colour scale show the number of cells per bin.

obtained similar results to ours, their variable clumping factor model (see Section 2.4, equation 3) compensates for omitted H_2 formation in unresolved high-density gas regions without any calibration.

3.2 Star formation activity

3.2.1 SF history

In this section, we explore different SF schemes and assess the impact of the H_2 modelling. In Fig. 7, we show the SF history of four runs, which adopted different SF algorithms: standard (so-called c100), S, SH2, SH2_SR. They all use the J75 H_2 -dust scheme with $C_\rho = 100$, which best reproduces the high column density observations for this level of numerical resolution (Fig. 5). As shown in Table 1, the c100 run includes the standard SF model, while S and SH2 incorporate the ‘self-gravity’ scheme (Hopkins, Narayanan & Murray 2013; Hopkins 2015) with an independent and dependent probability on the H_2 fraction (f_{H_2}), respectively. Finally, SH2_SR includes the last algorithm and the stellar radiation feedback scheme (see Sections 2.5 and 2.6 for a detail description of these algorithms).

Our ICs assume an initial exponential disc, which quickly evolves spiral substructures. SF is high during the first 0.1 Gyr, and then relaxes as the disc settles into its semi-steady state in all runs. For the c100 run which assumes density and temperature thresholds for the SF recipe, the SFR history shows more significant oscillations with many peaks and valleys interspersed, due to the combined effects of SN feedback and adopted thresholds. This is because after a starburst, the release of SN energy into the nearest gas neighbours produces the heating and disruption of the cold dense gas clouds, quenching the subsequent SF activity until they dissipate the additional energy and meet the SF criteria again. In addition, since the generation of new stars takes place in dense regions, statistically this process involves particles that are located in nearby regions with similar thermodynamic properties, resulting in relatively synchronous event that can explain the saw-tooth pattern of the SFR history in c100 run.

On the other hand, although models with self-gravity conditions show a global SFR that resembles the previous simulation, their SF activities are smoother over time so that the gas is depleted more slowly. Consequently, in the initial stages, they have SFRs smaller than c100. Additionally, the SFRs decline less abruptly with time. Hence, after ~ 0.35 Gyr, this trend is reversed and the SFRs of simulations S and SH2 become systematically larger and more spatially extended than that of c100. We should point out that we run all simulations for 2 Gyr in order ensure that 1 Gyr is indeed a

representative time of their equilibrium state. The smooth behaviour of the SF history in SH2 is affected by the stellar radiative feedback as shown in SH2_SR run. This radiation also heats and dissipates the cold and dense clouds in the ISM, and plays a major role in affecting the molecular content of the immediately contiguous gas clouds due to the significant increase of the H_2 dissociation rate. This effect lasts for short periods of time, corresponding to the lifetime of massive stars (≤ 0.03 Gyr), which are the main sources of FUV radiation. The lower H_2 fractions produce the decrease of the SFR in these regions, but the rate recovers again as the radiation from massive stars decreases over time.

3.2.2 Comparison of H_2 abundances with observations

In Fig. 8, we show the H_2 column density as a function of the total column density for S, SH2, and SH2_SR, compared to observations as in Fig. 5. The inclusion of self-gravity in the SF algorithm did not significantly modify this distribution compared to c100 (Fig. 5). Similarly, weighting the SF algorithm by the H_2 abundances produces comparable distributions in general. However, SH2_SR better reproduces the H_2 column density fractions for low column densities and exhibits a jump in their distribution at $\log[2N_{H_2}/(N_H + 2N_{H_2})] \sim -3$. This jump is probably the result of the abrupt H_2 turn-on due to the effects of self-shielding (Wolfire et al. 2008). At highest values of FUV radiation, the f_{H_2} is lower due to the rapid H_2 photodissociation. As the cloud column density (and thus τ) increases, the local FUV field drops due to dust extinction. In addition, the self-shielding by H_2 raises the f_{H_2} even more as the column density increases. The treatment of radiative stellar feedback regulates the production of H_2 as a function of total column density reproducing fractions which are more comparable to observational data. This is in agreement with Gillmon et al. (2006) and Shull et al. (2021), although a more detailed comparison with the MW observations is beyond the scope of this paper.

In addition, Fig. 9 shows less dispersion in the distribution of R_{mol} in SH2_SR while still reproducing the observed data. However, in the outermost regions of the simulated galaxy ($r/r_{83} \gtrsim 0.8$) there is still an excess as in the rest of the experiments executed with constant C_ρ (Fig. 6). In fact, the only experiment that better reproduces this observational relation is the run with variable C_ρ . The objective of this parameter is to compensate for the possible formation of H_2 in high-density regions which are not numerically resolved. However, a constant value is equally applied to every region, even where lower density is well resolved. Our results suggest that a variable C_ρ , which

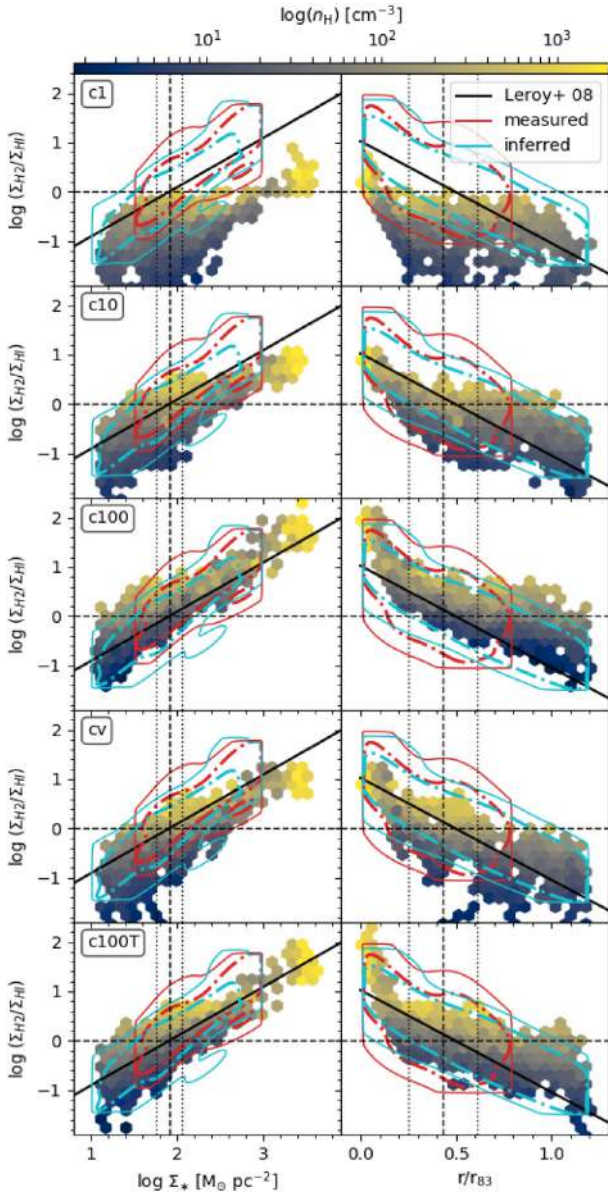


Figure 6. H₂-to-HI ratio, $R_{\text{mol}} = \Sigma_{\text{H}_2}/\Sigma_{\text{HI}}$, as a function of Σ_* (left) and radius (right). The continuous black lines are the Leroy et al. (2008) fits of R_{mol} and the contours enclose the 50 and 95 per cent of their observational data. The red contours enclose the pixel-by-pixel measurements of R_{mol} in spirals and the cyan contours contain points obtained from tilted rings in spiral galaxies with R_{mol} inferred from Σ_{SFR} and Σ_{HI} assuming a fixed SFE(H₂). The horizontal dashed lines show $R_{\text{mol}} = 1$. The vertical dashed lines are the values of Σ_* (left-hand panels) and radius (right-hand panel) estimated by Leroy et al. (2008) at which the HI-to-H₂ transition takes place (the vertical – dotted lines represent the standard dispersion).

takes into account the thermodynamical properties of the gas, might be the best option (Lupi et al. 2018). We will explore this in a future work.

Nevertheless we must also consider that we are comparing our simulated galaxies that are gas-rich systems with spiral galaxies observed at $z \sim 0$, which have much lower total gas fractions and column densities. So, high- R_{mol} values at large radii, coming from very massive clumps as we can see in Figs 1, 2, and 10 (face-on view), could be a feature of more gas-rich and clumpy galaxies that are more frequent at $z \sim 2$.

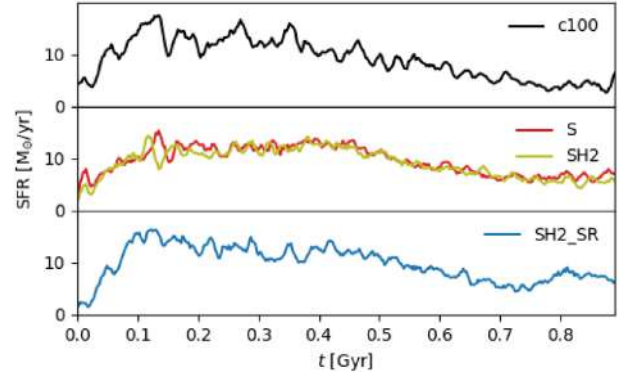


Figure 7. The SF histories of runs with different SF algorithms: standard (c100; upper panel), ‘self-gravity’ method (S; red) and ‘self-gravity’ method with the SF probability dependent on H₂ fraction (SH2; olive – middle panel), and the last recipe including stellar radiation feedback (SH2_SR; lower panel). All of them have been run with J75 dust model and $C = 100$.

The spatial distributions of the gas properties and Σ_{SFR} showed in Fig. 10 are slightly different among the three experiments. The S run shows a wider and more open spiral pattern for Σ_{HI} while the SH2 and SH2_SR runs present a tighter spiral structure where the HI is more extended. This is because most of H₂ content resides in the coldest and densest regions of the arms, promoting the SF activity only in these areas. Therefore, the molecular gas has shorter depletion times (defined as $\tau_d = \Sigma_{\text{SFR}}/\Sigma_{\text{H}_2}$) than similar regions in the S run. Nevertheless, in SH2_SR the aforementioned H₂ spatial distributions are more dispersed than in SH2, although it shares with the latter simulation the same SF recipe (i.e. associated with molecular clouds). Furthermore, due to the dissociating action of the stellar radiation from young stars, the molecular gas regions are slightly more extended and less dense, which translates into a weaker star formation activity in these regions.

Similarly, Byrne et al. (2019) using simulations of isolated disc galaxies and cosmological simulations of dwarf galaxies, compared a shielding-based SF model (i.e. coupling the SF probability to the amount of dust shielding) to a H₂-based model and to a temperature ceiling model. The comparison with the H₂-based recipe shows that the main difference is the SF at higher temperatures and lower densities found in the shielding-based scheme, which requires higher densities than the temperature-ceiling model to have active SF, on average. As in our simulations, one consequence of the different star-forming gas densities is the presence of denser gas in the run using the H₂ scheme, which also leads to more pronounced gas spiral structure. This can be explained by the time delay needed to form H₂ prior to SF. During that time, the gas can also collapse gravitationally and reach higher densities before spawning a star particle. Models without an explicit link between H₂ and SF, allow earlier formation activity while the gas is at a lower density.

3.3 The Kennicutt–Schmidt (KS) Law

In this section, the KS law is used to test the performance of our models. Fig. 11 shows Σ_{SFR} as a function of total gas surface density (Σ_{gas}), Σ_{H_2} , and Σ_{HI} for four experiments. They all assume the J75 scheme for H₂-dust formation. Two of them (c1 and c100) employ the standard SF scheme with $C_\rho = 1$ and $C_\rho = 100$, respectively, while SH2 and SH2_SR adopt the SF scheme based on the ‘self-gravity’ criterion and H₂-dependent probability for SF scheme (with $C_\rho = 100$). SH2_SR also includes the stellar radiation feedback.

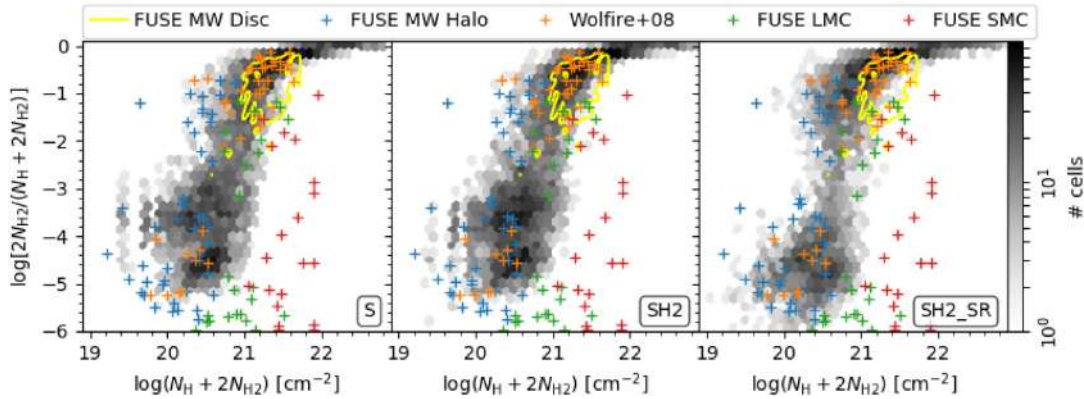


Figure 8. Observational comparisons of H_2 column density fractions for runs S (standard SF), SH2 (H_2 -dependent SF), and SH2_SR (H_2 -dependent SF and stellar radiative feedback). Symbol codes are given in Fig. 5.

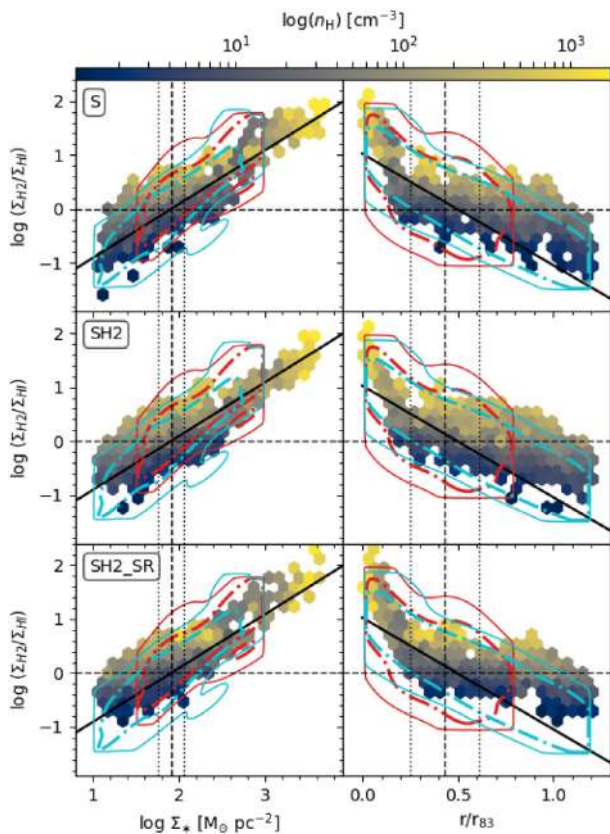


Figure 9. Observational comparisons for runs S, SH2, and SH2_SR. H_2 -to-HI ratio as a function of Σ_* (left) and radius (right). See Fig. 6 for details.

To compare with observations, we take the data of Schruha et al. (2011) from a sample of 33 nearby star-forming disc galaxies, with a mean metallicity of $12 + \log(O/H) \sim 8.7$ dex ($\sigma = 0.14$ dex). This is similar to the metallicity of our simulated galaxy measured at the r_{83} , $12 + \log(O/H) \sim 8.57$ dex. These authors focus their analysis on data stacked in bins of galactocentric radius, specifically in 15 arcsec wide tilted rings. This width varies depending on the source distance. For our comparison we adopt ~ 220 pc for its closest objects (3 Mpc). We employ a similar radial binning strategy, computing surface densities up to $1.2r_{83}$ (~ 12 kpc) in 200 pc wide concentric rings. Then, the colour scale in Fig. 11 indicates the mean H_2 -to-HI surface density

ratio for each bin, and the size of the cells showing the distribution of the simulated data represents the number of contributions to each bin

We found the $\Sigma_{SFR} - \Sigma_{gas}$ relation to be in very good agreement with observations by Bigiel et al. (2008, 2010, red contours in Fig. 11). These authors defined three different SF formation regimes in the $\Sigma_{SFR} - \Sigma_{gas}$ plane (delimited by vertical dashed lines). The first zone is dominated by HI up to a saturation threshold of $9 M_\odot pc^{-2}$. The second one is dominated by H_2 and the third one corresponds to the starburst activity. The last two regimes are delimited by a transmission band of around $200 M_\odot pc^{-2}$, where by increasing the density, the free-fall time is reduced within the gas cloud and can probably generate a more efficient SF activity. In addition, we include the literature measurements collected by Bigiel et al. (2008).

In the analysed models, the simulated $\Sigma_{SFR} - \Sigma_{gas}$ relation reproduces the lower threshold for SF, and also the trends for normal spirals as well as starbursts galaxies, which indicates that they exhibit a strong SF activity, in some of their regions, in agreement with the trends presented by the temporal evolution of their SFRs (Fig. 7). The KS-law obtained by using Σ_{gas} is almost unaffected by the clumping factor. However, the H_2 -to-HI ratio varies significantly because of the impact on the molecular formation. The molecular KS-law is displaced by roughly an order of magnitude between c1 and c100. This result suggests that the sub-grid clumping factor is working as we expected, allowing us to improve the performance of our model in the very high density regions for the resolution of this IC (Gnedin et al. 2009; Lupi et al. 2018). Furthermore, for c100, the transition zone ($\log(H_2/HI) \sim 0$) is narrower than that of SH2, which is narrower than that SH2_SR. For the last two schemes, this behaviour can be explained by the H_2 dependence of the SFR algorithm, and by the presence of the radiative feedback that causes the destruction of molecular hydrogen.

The molecular KS law ($\Sigma_{SFR} - \Sigma_{H_2}$) is also explored. With a clumping factor $C_\rho = 100$, this correlation follows very well the observed one, following the lines of constant depletion time (i.e. defined as the inverse of SFE) for $\tau_d \sim 2$ Gyr (Bigiel et al. 2008; Leroy et al. 2008), in agreement with observations for normal spiral galaxies (e.g. Gao & Solomon 2004; Schruha et al. 2011). With this C_ρ , the KS-law is also well reproduced for the lower density tail of Σ_{H_2} . Similar behaviours are detected for SH2_SR although these relations show slightly larger scatter that contributes to better match the observed contours. Bigiel et al. (2008) interpret the linear relation and constant depletion times as evidence for approximately uniform

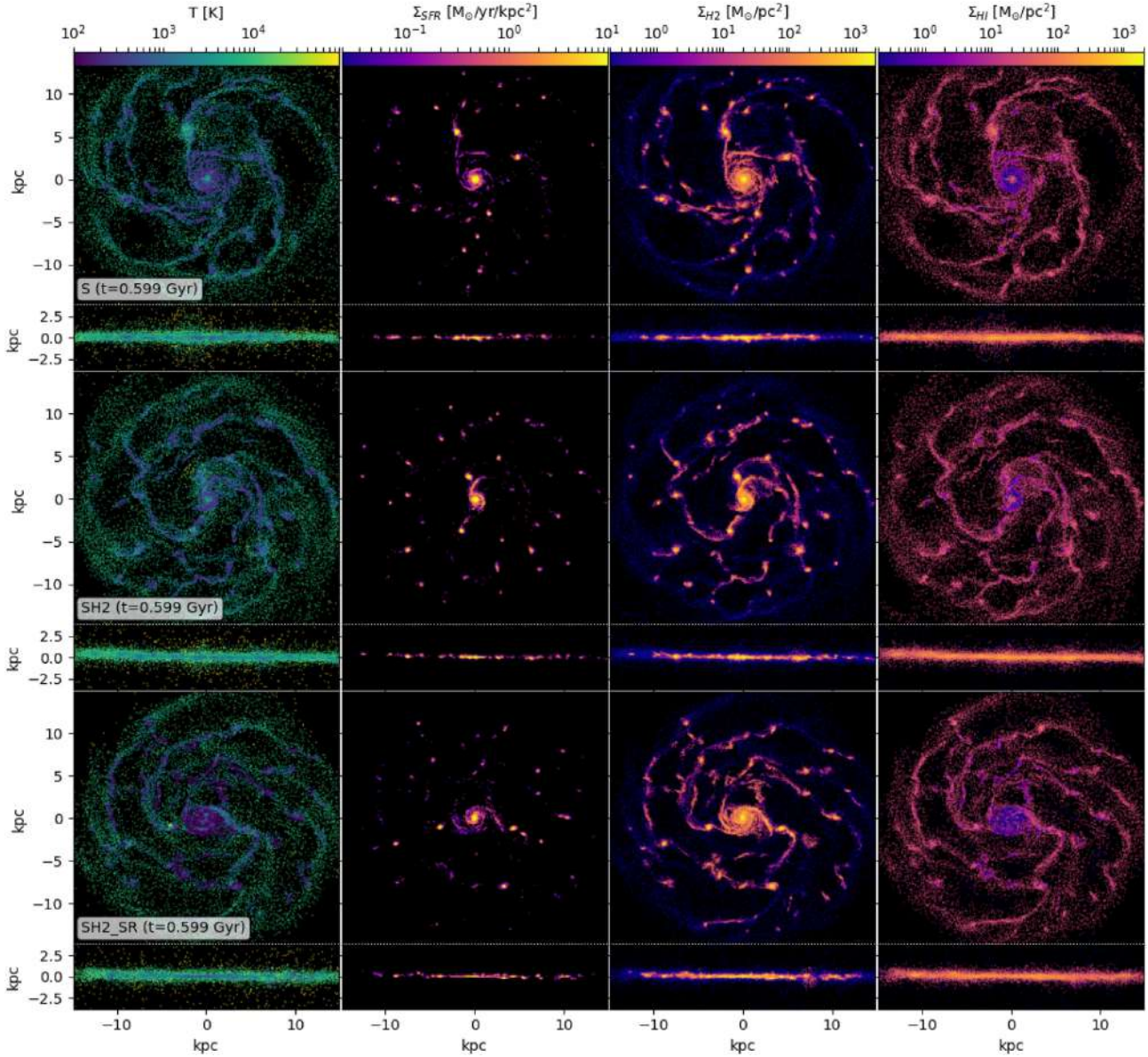


Figure 10. Face-on and edge-on maps of S (upper panels), SH2 (middle panels), and SH2_SR (lower panels) simulations that adopts different SF algorithms as described in Section 2.4. See Fig. 1 for a detailed description.

SF activity in giant molecular clouds. These authors also suggest that Σ_{H_2} may be a better measure of the filling fraction of GMC than of the changing conditions in the molecular gas.

For high-density regions, our models overestimate the Σ_{SFR} with respect to a constant τ_{d} , overlapping with the starburst regime. In fact, as can be seen in Fig. 11, the agreement with observational data of luminous and ultraluminous infrared galaxies (LIGs/ULIGs) (Gao & Solomon 2004) is remarkably good.

The difference between SH2 and SH2_SR models is mainly limited to larger dispersion in the distributions of the latter, as exhibit their surface density distributions represented by the cell sizes in Fig. 11. This reflects the dissociating effect of stellar radiation, although it has a weak impact on the global trend. Nevertheless, due to the similarity between both models, further studies are required to understand whether the correlation between SF and H_2 content implies causality.

Byrne et al. (2019) reported similar results for their SF schemes, since all of them are consistent with the KS law with only slight differences with the observable properties of the resulting galaxies. However, these authors claim that their effects would be stronger in simulations focused on the very early universe or capable of resolving the internal structure of star-forming clouds.

Finally, the $\Sigma_{\text{SFR}}-\Sigma_{\text{H}_1}$ relation agree with observational results reported by Bigiel et al. (2008, 2010) and Schruba et al. (2011). Our initial condition for the disc component, including the stellar and gas phase, follows an exponential profile. Since simulated galaxies evolve in isolation without experiencing any external disturbance, we can assume that the initial exponential profiles imprinted in the stellar and gas components does not undergo significant changes, so that the internal regions are on average denser than the external ones and therefore they satisfy the conditions to form stars sooner and more efficiently. Indeed, the higher level of SF activity corresponds

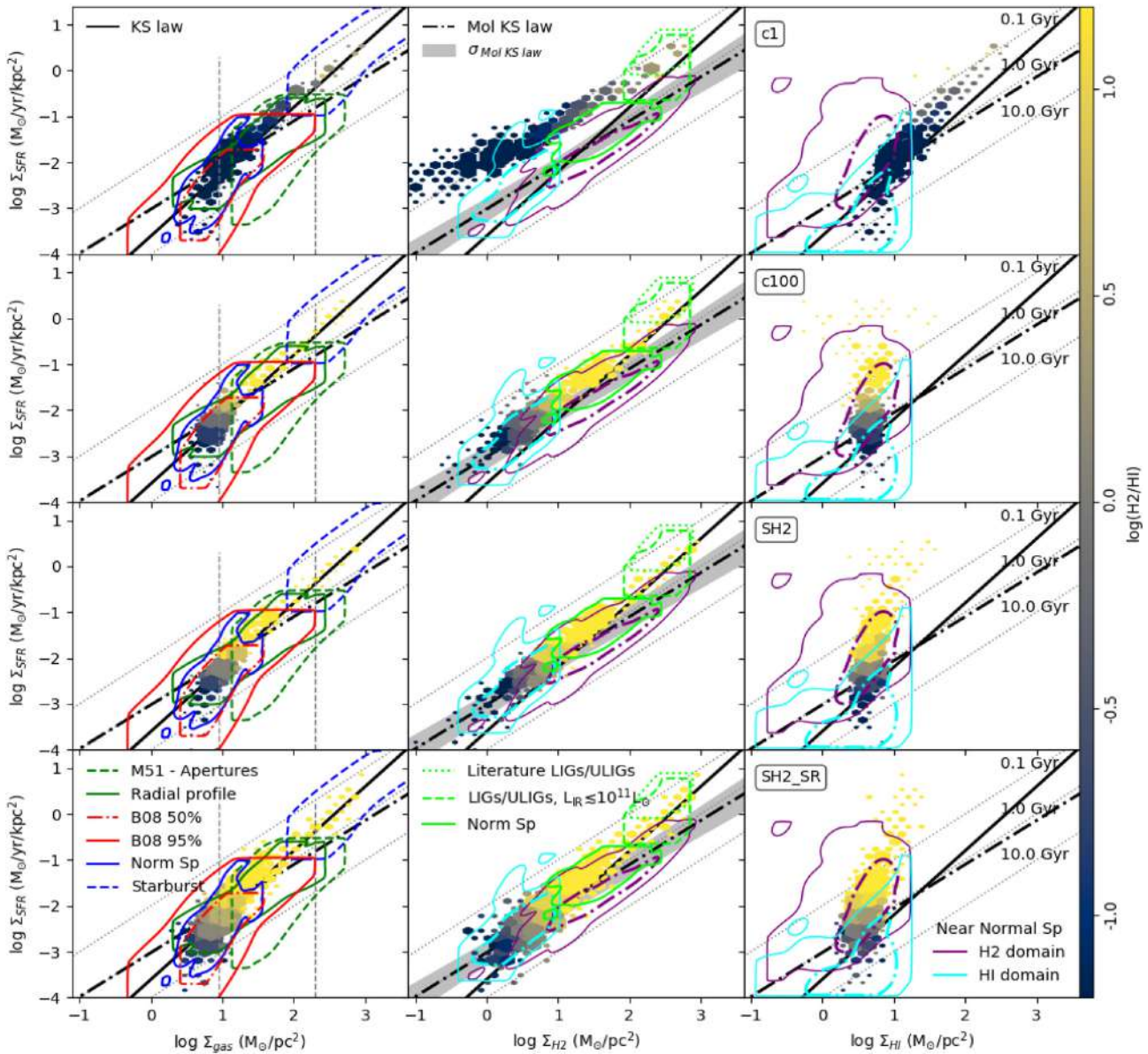


Figure 11. KS law for c1, c100, SH2, and SH2_SR. We show the average relation for the total gas, H_2 , and $H1$ only, and compare them with the original (KS, solid black line) and molecular (mol-KS, black dash-dotted line) KS law. The grey band in the central column, is a dispersion of 1σ for the mol-KS law estimated by Bigiel et al. (2008) and the red contours in the first column enclose the 50 (dashed) and 95% (solid) of their observational data. While the dashed grey vertical lines delimit three different regimes of SF formation defined by them. Also in the first column, the additional contours enclose 95% of: measurements in individual apertures (green dashed) in M51 (Kennicutt et al. 2007), data points from radial profiles (green solid) from M51 (Schuster et al. 2007), NGC 4736, NGC 5055 (Wong & Blitz 2002), and NGC 6946 (Crosthwaite 2007). Furthermore, we include the disc-averaged measurements from normal spiral (blue solid) and starburst galaxies (blue dashed) from Kennicutt (1998). In rest columns, the contours contain the 50% (dash-dotted) and 95% (solid) of data of Schruha et al. (2011) for H_2 (violet) and $H1$ (cyan) dominated regions. And, in the middle columns, the green contours enclose the 95% of data of Gao & Solomon (2004), for ULIGs available from literature (dotted), LIGs and ULIGs with $L_{IR} \lesssim 10^{11} L_{\odot}$ (dashed) and less luminous normal spiral galaxies (solid). In all panels, the overplotted diagonal black dotted lines correspond to 0.1, 1, and 10 Gyr constant depletion times (defined as $\tau_d = \Sigma_{SFR}/\Sigma_X$, with $X = H1 + H_2, H_2$, or $H1$), the colour scale points out the mean H_2 -to- $H1$ surface density ratio for each bin and the size of the cells showing the distribution of the simulated data represents the number of data within each of these.

to the central regions in these experiments. Bigiel et al. (2008, 2010) found that SF in outer disc regions is very inefficient compared to SF inside the optical discs. In addition they observed $H1$ depletion times of 100 Gyr for most of their data, and regions with local $\tau_d < 10$ Gyr are rare to find. The disagreement with our simulations at low gas densities ($\lesssim 3 M_{\odot} pc^{-2}$) seems to indicate that further adjustment of our chemical model and/or the SF scheme is required to improve the modelling at very low gas densities.

Bigiel et al. (2010) conclude that, on average, outer disc contribute only about 10 per cent to the total SFR of a galaxy and the lack of importance of *in situ* SF means that the massive extended gas distributions observed in many nearby galaxies can be interpreted as a potential fuel source for inner disc SF. The short depletion times in these regions ($\tau_d \sim 2$ Gyr) imply that this source is required as well as the presence of mechanisms such as radial gas flows that replenish the innermost areas.

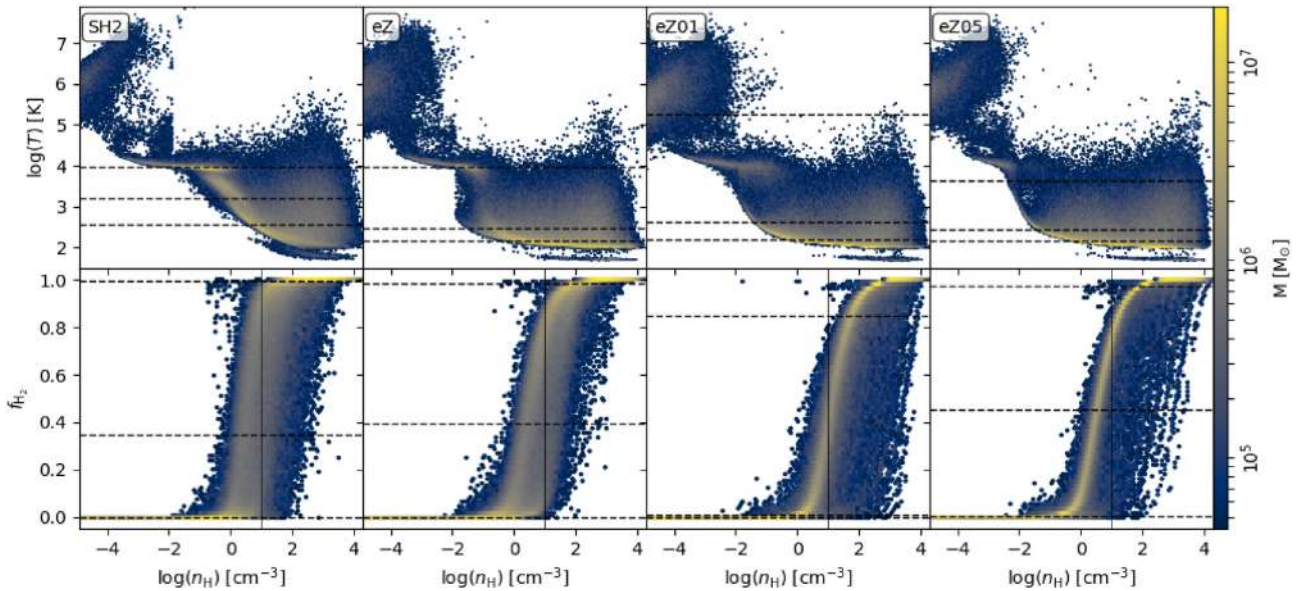


Figure 12. Temperature and H₂ mass fraction as a function of n_{H} (cm^{-3}), for SH2, eZ, eZ01, and eZ05 (left to right, respectively). The dashed lines indicate the 25, 50, and 75 percentiles for the distributions of temperature (upper panels) and f_{H_2} (lower panels). The vertical line denotes $n_{\text{H}} = 10 \text{ cm}^{-3}$.

3.4 Dependence on metallicity

In this section, we analyse the dependence of H₂ formation on gas metallicity. Our goal is to understand the effects of considering a fixed metallicity for the gas or a self-consistent chemical enrichment by SNaE that produce the variation of the gas metallicity over time. All the experiments discussed in this section adopt the self-gravitation model with H₂ dependence (see Table 1).

We performed two different experiments adopting a uniform distribution of chemical abundances per gas particle, consistent with a metallicity of 0.1 (eZ01) and 0.5 Z_{\odot} (eZ05). However, this condition obstructs us from implementing non-equilibrium metal cooling schemes for $T < 10^4$ K, because fixing the metallicity prevents the evolution of the numerical densities of the metal species relevant for cooling as required by our scheme. To solve this, we extended the equilibrium metal cooling range to $T < 10^4$ K, following Lupi et al. (2018). This scheme was implemented for these two experiments and a third run (eZ) that uses the full chemical evolution model. eZ includes SNI and SNIa enrichment and our initial ad hoc metallicity profile (see Section 2.7). The later run is used as a benchmark to assess the effects of assuming the fixed abundance under similar conditions for the cooling process.

There are several physical phenomena linked to the level of chemical enrichment in the gas phase. Metal cooling increases with metallicity because of the enhanced free electron density. In our equilibrium scheme, it scales linearly with Z (Shen et al. 2010, 2013). High metallicities also imply high dust-to-gas ratios, which in this work are assumed to scale as $D = D(Z/Z_{\odot})$ (see Section 2.4). Consequently, we also expect a larger abundance of molecular hydrogen, and stronger molecular-hydrogen cooling (which, however, at the densities and metallicities considered in this work, is subdominant with respect to metal cooling). In agreement with the above expectations, the gas density–temperature diagrams (top panel of Fig. 12) show how the cold gas fraction increases with increasing metallicity (the dashed horizontal lines depict the gas temperature reached by the 25, 50, and 75 per cent of the gas mass).

In particular, both eZ01 and eZ05 show the denser 25 per cent of total gas mass located below $\sim 3 \times 10^2$ K, in the H₂-dominated region, whose contribution to the gas cooling is relevant. The denser 50 per cent of cold gas mass also spans similar ranges of density in both simulations but in eZ05 it is colder than in eZ01, where this gas is below $\sim 4 \times 10^2$ and $\sim 7 \times 10^2$ K, respectively. Finally, the temperatures of gas mass distributions from 50 to 75 percentiles show larger differences, since in eZ05 they do not exceed the $\sim 5 \times 10^3$ K while in eZ01, achieve $\sim 1 \times 10^5$ K. In the lowest metallicity model (eZ01), there is a weaker impact of metal cooling and also of H₂ cooling due to the lower H₂ mass formed. However, comparing eZ with eZ01 and eZ05 below 10^3 K and for high-density regions, we note that the direct dependence of the cooling processes on metals does not appear to be very strong. As we can see in the lower panels of Fig. 12, the impact of metallicity on the H₂ abundance at a given n_{H} is very clear for the higher metallicity run.

As expected from the direct link between metallicity, dust, and H₂ formation, the range of densities at which the gas starts transitioning from atomic to molecular (i.e. the transition zone) slightly shifts towards lower densities with increasing metallicity and becomes more concentrated (Christensen et al. 2012). In our experiments these changes are small since the difference in metallicity between both simulations is only a factor of five. Nevertheless, the amount of gas with high f_{H_2} increases. For example, ~ 25 per cent of the gas mass has a $f_{\text{H}_2} \gtrsim 0.90$ for eZ01 and $f_{\text{H}_2} \gtrsim 0.96$ for eZ05, while 50 per cent of gas mass has $f_{\text{H}_2} \gtrsim 0.10$ and $f_{\text{H}_2} \gtrsim 0.50$ for each simulation, respectively (see dashed lines in lower panels of Fig. 12). We also note a wide spread of densities in the region of gas transitioning from atomic to molecular.

If we focus on SH2 and eZ (first two columns in Fig. 12), we find that a metal cooling process assuming thermochemical equilibrium substantially affects the n_{H} and temperature distributions mainly at low densities, e.i. $n_{\text{H}} \lesssim 10 \text{ cm}^{-3}$. We recall that this n_{H} threshold denotes the mean density of the transition zone between H I and H₂. However, for the higher n_{H} there are not large changes in the H₂ fractions. This can be explained because the main formation channel

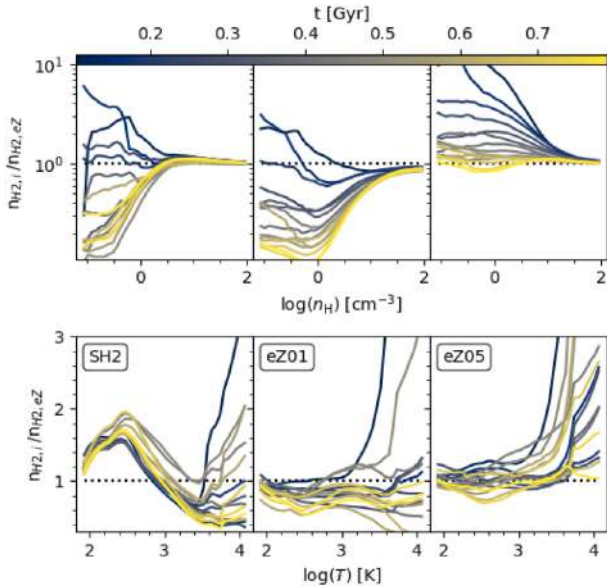


Figure 13. Temporal evolution of the H_2 abundances ratio ($n_{H_2,i}/n_{H_2,eZ}$) of $i = \text{SH2, eZ01, and eZ05}$ models with respect to eZ as function of n_{H_1} (upper panel) and the temperature (lower panel). The dotted line indicates when the H_2 abundance of each model is equal to that of eZ ($n_{H_2,i}/n_{H_2,eZ} = 1$).

for H_2 is the catalysis on the surface of the dust which depends on the metallicity and n_{H_1} .

In addition, comparing the temporal evolution of SH2 (which has an initial metallicity gradient corresponding to an average gradient observed for $z = 2$) with a simulation that starts with primordial gas (LR, see Table 1), we observe that the latter requires ~ 0.45 Gyr to reach a Σ_{H_2} similar to that of SH2 in $r < 0.5r_{83}$, while for $r > r_{83}$ displays a Σ_{H_2} always smaller (for a factor of ~ 5) for at least 2 Gyr.

A more quantitative analysis is shown in Fig. 13. Here, for each model (SH2, eZ01, and eZ05), we calculate the distribution of H_2 number density normalized by the corresponding value in eZ ($n_{H_2,i}/n_{H_2,eZ}$; i denotes the different models) as a function of the temperature and the n_{H_1} for different evolution times. We compare these distributions, evaluating the ratio of H_2 abundance and the time variation. We remark that, in addition to employing thermochemical equilibrium cooling rates, eZ includes the full chemical evolution driven by SN feedback so that the metallicity of the ISM will increase with time.

First, we compare the evolution of the n_{H_2} between SH2 and eZ which allow us to evaluate the impact of non-equilibrium cooling. As it can be seen from Fig. 13 (left-hand panels) as a function of n_{H_1} there are no significant differences for $n_{H_1} > 10 \text{ cm}^{-3}$. However for lower densities, eZ underestimates the H_2 production in the initial times, but as the enrichment increases with the temporal evolution of the system, eZ begins to overestimate the H_2 content. For $T \lesssim 1000$ K, eZ underestimates n_{H_2} while overestimating it for higher temperatures (except for a short short period of ~ 0.1 Gyr, from 0.4 to 0.5 Gyr).

For eZ01 and eZ05, we observe that the production of H_2 in very dense and cold regions is similar in all cases. This indicates that these regions are prompted to molecular H formation regardless of metal abundance. However, as Capelo et al. (2018) also observed, if we consider lower density regions, the metallicity begins to play an important role due to its influence on the schemes chosen here to model the H_2 formation in dust. Thus, as the metallicity increases in eZ (due to SN feedback), its H_2 production evolves

approaching that of eZ05 and moving away from eZ01. As a function of the temperature, we find again that the H_2 abundance rises with increasing metal content and exhibits a large dispersion as shown in Fig. 13. However, the larger impact of metallicity on the synthesis of H_2 is detected in regions with temperatures $T \gtrsim 1 \times 10^3$ K, while in very cold and dense regions ($T \lesssim 1 \times 10^3$ vK) the effects are less important. This indicates that for the H_2 formation in the aforementioned cold and dense areas, the dominant process is the H_2 catalysis on the dust grains surface. As the models used for this mechanism assume a direct proportionality with Z/Z_\odot and n_{H_1} , then at high-density regions ($n_{H_1} \gtrsim 10$) the last quantity dominates widely over the metal abundances ($Z_\odot \lesssim 1$) (see Section 2.4).

Finally, we consider the impact of metallicity and H_2 formation on the morphology and spatial distribution of H_2 in gas-phase disc (not shown here, see fig. A in supplementary online material). The models with fixed metallicity all over the discs (eZ01 and eZ05) show a more widespread molecular formation. This is related to the temperature pattern shown in Fig. 13 in which low temperatures extend more evenly and to the outermost disc regions for higher metallicities. We can still individualize stellar and molecular formation in clumps. However, compared to the SH2 model (Fig. 10), these are smaller and more tenuous, and are found in large numbers and more evenly distributed across the disc.

3.5 Considerations on numerical resolution

In order to analyse the impact of numerical resolution, we present the results of two runs with different resolution, hereafter high (HR) and low (LR) resolution. The ICs for this analysis are described at the end of Section 2.7. Simulations start from primordial gas without adopting an initial metallicity gradient and these simulations used our best model: SH2 and J75 schemes, with $C_\rho = 10$ and 100 for the HR and LR, respectively (see Table 1). Recall that the clumping factor is introduced to take into account the effects of limited numerical resolution. Hence, for the HR run a lower value, $C_\rho = 10$, is required in order to reproduce observational trends (Fig. 14).

For simplicity, we do not include the complete analysis carried out for low-resolution runs, but these studies have been fully done on the HR run. Instead, we limit the discussion to examine and contrast the radial distributions of total gas, H I, H_2 , and the SF activity present in LR and HR (Fig. 15), and the behaviour of the KS laws (Fig. 16). Our goal is not to reproduce any specific galaxy, but to evaluate the impact of numerical resolution using our reference model to ensure that our trends are robust.

We compare the radial profiles of H_2 and SFR estimated for our simulations with the observational ones by Leroy et al. (2008) and Gallagher et al. (2018). The general trend in these observations is that the both profiles reach the maximum densities in the galactic centre and decay to the outskirts of the disc, while H I is approximately constant across the disc. Our results are in very good agreement with the observations and since the clumping factor differs by an order of magnitude between the two runs, it is clear that an increase in resolution affects the model of H_2 formation on dust, since higher density regions can be better resolved as well as the chemical processes that take place in them. However, the tuning of this parameter allows us to recover a good match with observations.

Additionally, the H_2 and SFR profiles and their evolution are very similar in the two simulations, on average. By looking in detail, we note that initially, the surface density of H_2 exceeds that of H I, which increases slightly as the system evolves. In addition, the SFR of the LR run reaches marginally higher values in the central region than HR, and falls faster in the intermediate disc regions. Probably, these

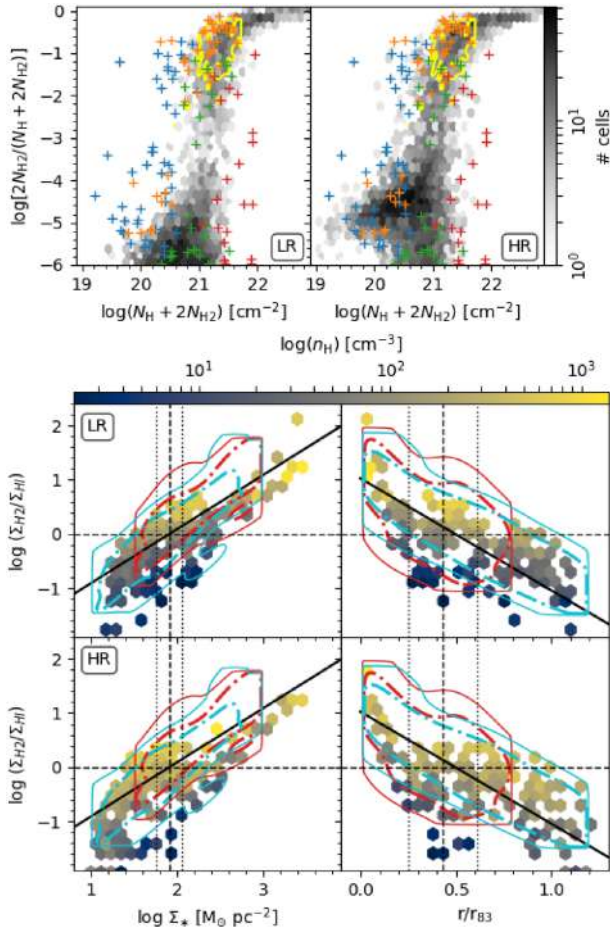


Figure 14. Observational comparisons for runs LR and HR. Top panels: H_2 column density fraction (Idem Fig. 8). Bottom panels: H_2 -to- $H\text{I}$ ratio, $R_{\text{mol}} = \Sigma_{H_2}/\Sigma_{H\text{I}}$, as a function of Σ_* (left) and radius (right – Idem Fig. 9).

higher central SFRs, on average, are due to the limitations imposed by the resolution, which establishes the mass of each gas particle that will form new stars, obtaining a formation in discrete quantities whose stellar mass is greater for lower resolutions. As the numerical resolution improves, this effect weakens and the simulation better reproduces observed distributions of the H_2 column density fractions and the H_2 -to- $H\text{I}$ ratios as a function of Σ_* and radius (see Fig. 14). However, in both simulations, the H_2 profile reaches its peak in the galactic centre and falls towards the outer disc, while the $H\text{I}$ profile remains relatively flat throughout the disc. The SFR also peaks in the centre and trends in its profile largely follows those of H_2 . Finally, the stellar distributions are very similar for both resolution runs.

Hence, these trends show that, although the distributions of chemical species ($H\text{I}$ and H_2) and star-forming regions are slightly smoother with increasing resolution, both runs provides similar distributions which are globally consistent with observations.

4 SUMMARY

In this work, we developed a new implementation of P-GADGET3 that includes the chemistry package KROME. P-GADGET3-K allows a self-consistent description of H_2 formation as baryons cool and form new stars while the ISM is chemically enriched by SNIa and SNII. Our code considers energy feedback by SNaE, an extragalactic UV and local stellar radiation fields. We run a set of isolated galaxies

to evaluate the performance of P-GADGET3-K and the relevance of different physical prescriptions and their free parameters (H_2 formation via dust grains, clumping factor, and metallicity) as well as the impact of H_2 on SF activity. Special care was given to the initial gas metallicity so that the gas component starts with a metallicity profile in agreement with observations at $z \sim 2$, considering that chemical abundances affects both the cooling rates and H_2 formation. We explore two possible models for the formation of H_2 via dust grains, Jura (1975) and Tomassetti et al. (2014).

Our results can be summarized as follows:

(i) We find that the characteristics of simulated systems are in very good agreement with a variety of observable properties of molecular gas (Fig. 6). R_{mol} covers a similar range of values as observations and behaves as a continuous function spanning from the H_2 -dominated (~ 10) to $H\text{I}$ -dominated (~ 0.1) regions of the ISM. Particularly, for the adopted numerical resolution, the runs with $C_\rho = 100$ show the best fits to observational distributions as a function of Σ_{SFR} and effective radius (Fig. 6).

The H_2 fraction is comparable to the observations on average (Fig. 5), although the T14 dust model is found to produce less H_2 at a given N_{H} . As expected the profiles of Σ_{H_2} , $\Sigma_{H\text{I}}$, and Σ_{SFR} vary with the clumping factor and numerical resolution. The ISM in the standard experiments with low (< 100) or variable (cv) clumping factor are more dominated by $H\text{I}$ and they do not fit these observations well. On the other hand, the observed range of column densities is better reproduced by the experiments with a variable C_ρ and J75 or a $C_\rho = 100$ and T14, that is, where the H_2 -dust schemes depend on some local thermodynamic properties of the gas. Therefore, in a future work, we will analyse in detail these schemes, seeking to understand the relationship between the clumping factor, the thermodynamical properties of the gas and the numerical resolution, to obtain guidelines for choosing the most appropriate model.

(ii) In our model with local stellar radiation field, SH2-SR, the simulated distribution of N_{H_2} with respect to $N_{\text{H}} + 2N_{H_2}$ improves and reproduce values within the entire observational range set by MW, LMC, and SMC. However, the Σ_{H_2} distributions or KS relations are not significantly different when compared to SH2, since the greatest impact of radiation occurs in less dense regions where the effects of attenuation and self-shielding are not dominant where star formation is less active.

(iii) We find a very good agreement between the abundances and distributions of $H\text{I}$, H_2 , SFR, and stellar mass of the LR and HR experiments (Figs 14 and 15). The effects of low resolution can be seen in the central regions where LR exhibits higher levels of activity. As expected, the HR required a lower clumping factor to reproduce observations.

(iv) The density–temperature diagrams show that simulated galaxies follow the same trends, on average, but the extreme values that the temperature and/or the density can reach depend on the chemical content and numerical resolution. This, together with the C_ρ , contribute to shape the phase diagrams for H_2 .

(v) We tested two different SF schemes and explore the gas behaviour and, the molecular and $H\text{I}$ KS laws. For the standard SF model, based on a density and temperature thresholds, we run experiments varying the clumping factor and the H_2 -dust model. Increasing the clumping factor generates an increase of the H_2 abundance as self-shielding is more efficient. This produces a molecular KS law with a slope slightly closer to the observed one, while the non-use of a clumping factor increases the differences between observations and simulations. We also found that the use

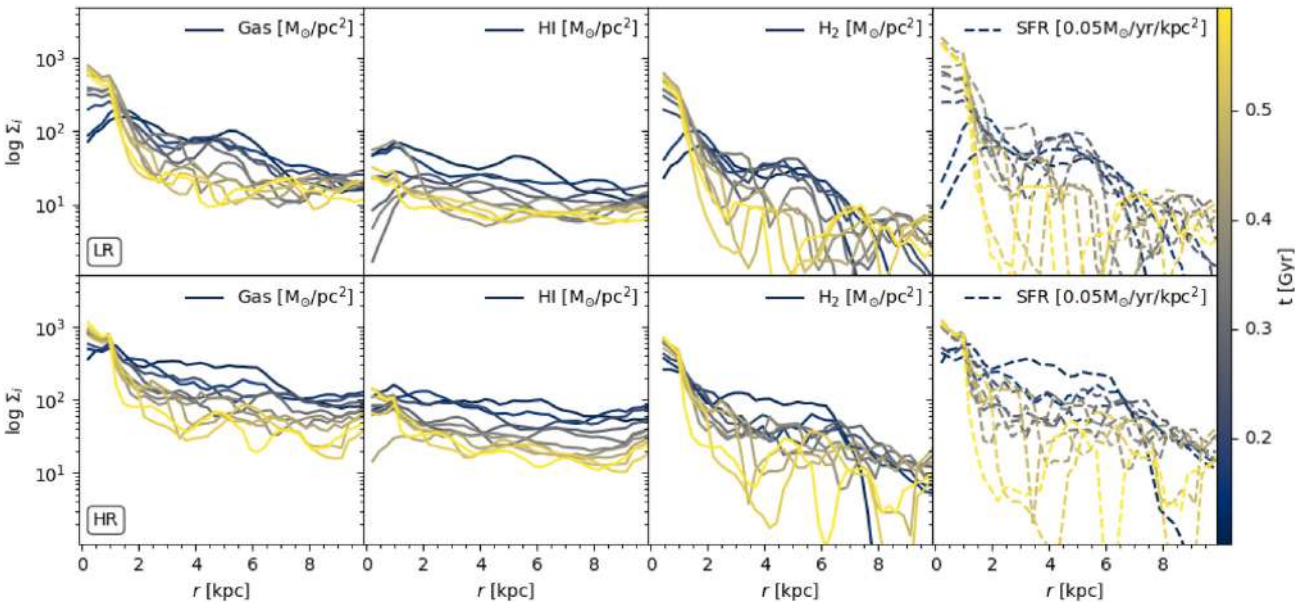


Figure 15. Surface density profiles of total gas, stars, HI, H_2 , and SFR for LR (upper panels) and HR (lower panels) experiments.

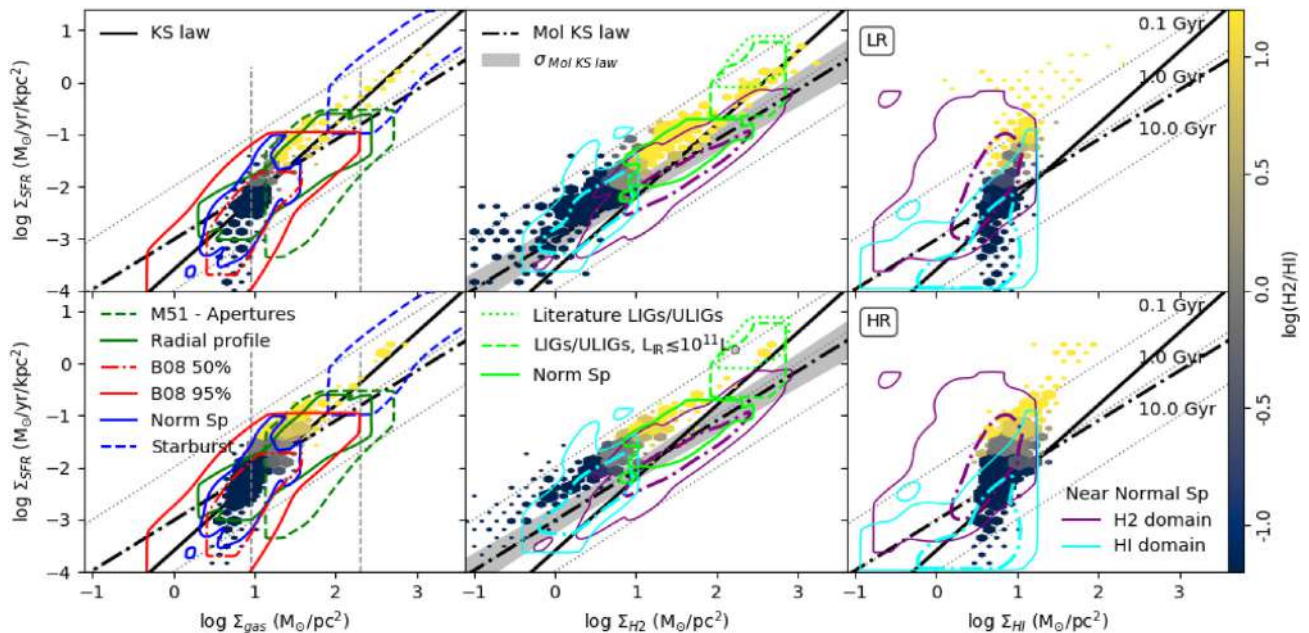


Figure 16. KS laws for runs LR (upper panels) and HR (lower panels). We show the average relation for the total gas, H_2 and HI only, and compare them with the original (KS, solid black line) and molecular (mol-KS, black dash-dotted line) KS law. Figure equivalent to Fig. 11 for a different set of models.

of the J75 scheme results in a larger fraction of H_2 than the T14 model, with the same clumping factor. The SFR history produced by the standard SF scheme shows fluctuating behaviour with many significant peaks and valleys interspersed. Nevertheless, the second model, based on the ‘auto-gravity’ criterion (Hopkins et al. 2013; Hopkins 2015) and a H_2 -dependent probability of SF, shows an SF activity smoother over time but with a similar global trend to the previous scheme. We do not find large differences in the SFR and global properties of ISM when using a H_2 -dependent SF algorithm. However, the SH2 and SH2_SR runs reproduce observational trends slightly better (Figs 8 and 9). This is encouraging given the sim-

ilarity of the algorithm and will be further analysed in a future work.

(vi) On the other hand, the modelling of the chemical evolution of metallic species (C I, C II, O I, O II, Si I, Si II, and Si III) and non-equilibrium cooling has a significant effect on gas thermodynamics, chemical abundances, and morphology of the galaxy, in agreement with previous works. Compare to a model that assumes thermochemical equilibrium, the non-equilibrium scheme produces a wider distribution of the gas with temperatures around $\sim 10^3$ K. It also generates higher fractions of molecular gas at low temperatures. The spatial distribution of the molecular components is more extended

in the non-equilibrium scheme. However, the differences in gas thermodynamics are typically small for the cold and dense regions where stars are formed, implying similar levels of SF activities.

(vii) As expected, the metallicity of gas has direct consequences on its cooling rates and the H₂ formation. A model with higher initial metallicity produces a colder gas and a larger fraction of molecular gas than one with primordial or low metallicity. However, the metal enrichment by SNaE tends to dilute the initial metallic discrepancy between runs. We find that the presence of a pre-set metallicity gradient allows a better description of the H₂-to-H I ratio and avoids the low-density tail in the molecular KS relation.

In summary, our updated code P-GADGET3-K is a powerful numerical tool that will allow us to address, in a more detailed and physical way, the regulation of SF and the gas cycle during galactic evolution.

ACKNOWLEDGEMENTS

The authors would like to thank the anonymous reviewers for their insightful comments. This work used the RAGNAR cluster, funded by Fondecyt 1150334 and Universidad Andres Bello, and the Geryon2 cluster at the Centro de Astro-Ingeniería UC. PBT acknowledges partial supports from Fondecyt 120073/2020 and the Galnet Network supported by CONICYT, and CATA. SB and DRGS thanks for funding via Conicyt PIA ACT172033. SB acknowledges support from Fondecyt Iniciación 11170268 and DRGS thanks for funding via Conicyt Programa de Astronomía Fondo Quimal 2017 QUIMAL170001. DRGS and SB acknowledge financial support from the Millenium Nucleus NCN19_058 (TITANs).

DATA AVAILABILITY

The data underlying this article will be shared on reasonable request to the corresponding author.

REFERENCES

- Abel T., Anninos P., Zhang Y., Norman M. L., 1997, *New Astron.*, 2, 181
 ALMA-Partnership, 2015, *ApJ*, 808, L1
 Aoyama S., Hou K.-C., Shimizu I., Hirashita H., Todoroki K., Choi J.-H., Nagamine K., 2017, *MNRAS*, 466, 105
 Arth A. et al., 2019, Astrophysics Source Code Library, record ascl:1909.011, preprint ([astro-ph/1907.11250](https://arxiv.org/abs/1907.11250))
 Bakes E. L. O., Tielens A. G. G. M., 1994, *ApJ*, 427, 822
 Balsara D. S., 1995, *J. Comput. Phys.*, 121, 357
 Beck A. M. et al., 2016, *MNRAS*, 455, 2110
 Bigiel F., Leroy A., Walter F., Brinks E., de Blok W. J. G., Madore B., Thornley M. D., 2008, *AJ*, 136, 2846
 Bigiel F., Walter F., Blitz L., Brinks E., de Blok W. J. G., Madore B., 2010, *AJ*, 140, 1194
 Blitz L., Rosolowsky E., 2006, *ApJ*, 650, 933
 Bolatto A. D., Wolfire M., Leroy A. K., 2013, *ARA&A*, 51, 207
 Bovino S., Grassi T., Schleicher D. R. G., Latif M. A., 2014, *ApJ*, 790, L35
 Bovino S., Grassi T., Capelo P. R., Schleicher D. R. G., Banerjee R., 2016, *A&A*, 590, A15
 Bromm V., Loeb A., 2003, *Nature*, 425, 812
 Bruzual G., Charlot S., 2003, *MNRAS*, 344, 1000
 Byrne L., Christensen C., Tsekitsidis M., Brooks A., Quinn T., 2019, *ApJ*, 871, 213
 Capelo P. R., Bovino S., Lupi A., Schleicher D. R. G., Grassi T., 2018, *MNRAS*, 475, 3283
 Catinella B. et al., 2018, *MNRAS*, 476, 875
 Cazaux S., Spaans M., 2004, *ApJ*, 611, 40
 Cazaux S., Spaans M., 2009, *A&A*, 496, 365
 Cen R., 1992, *ApJS*, 78, 341
 Chen Y., Bressan A., Girardi L., Marigo P., Kong X., Lanza A., 2015, *MNRAS*, 452, 1068
 Christensen C., Quinn T., Governato F., Stilp A., Shen S., Wadsley J., 2012, *MNRAS*, 425, 3058
 Crosthwaite L. P., 2007, *ApJ*, 134, 16
 Cullen L., Dehnen W., 2010, *MNRAS*, 408, 669
 Dame T., Hartmann D. H., Thaddeus P., 2001, *ApJ*, 547, 792
 Dehnen W., Aly H., 2012, *MNRAS*, 425, 1068
 Draine B. T., 2003, *ARA&A*, 41, 241
 Federrath C., Roman-Duval J., Klessen R. S., Schmidt W., Mac Low M.-M., 2010, *A&A*, 512, A81
 Ferland G. J., Korista K. T., Verner D. A., Ferguson J. W., Kingdon J. B., Verner E. M., 1998, *PASP*, 110, 761
 Forrey R. C., 2013, *ApJ*, 773, L25
 Frebel A., Simon J. D., Geha M., Willman B., 2010, *ApJ*, 708, 560
 Freeman K. C., 1970, *ApJ*, 160, 811
 Gallagher M. J. et al., 2018, *ApJ*, 858, 90
 Galli D., Palla F., 1998, *A&A*, 335, 403
 Gao Y., Solomon P. M., 2004, *ApJ*, 606, 271
 Genzel R., Stutzki J., 1989, *AR&AA*, 27, 41
 Gillmon K., Shull J. M., Tumlinson J., Danforth C., 2006, *ApJ*, 636, 891
 Glover S. C. O., 2015, *MNRAS*, 453, 2902
 Glover S. C. O., Abel T., 2008, *MNRAS*, 388, 1627
 Glover S. C. O., Clark P. C., 2012, *MNRAS*
 Glover S. C. O., Jappsen A.-K., 2007, *ApJ*, 666, 1
 Glover S. C. O., Savin D. W., 2009, *MNRAS*, 393, 911
 Gnedin N. Y., Kravtsov A. V., 2011, *ApJ*, 728, 88
 Gnedin N. Y., Tassis K., Kravtsov A. V., 2009, *ApJ*, 697, 55
 Goldsmith P. F., Heyer M., Narayanan G., Snell R., Li D., Brunt C., 2008, *ApJ*, 680, 428
 Grassi T., Bovino S., Schleicher D. R. G., Prieto J., Seifried D., Simoncini E., Gianturco F. A., 2014, *MNRAS*, 439, 2386
 Grassi T., Bovino S., Haugboelle T., Schleicher D. R. G., 2017, *MNRAS*, 466, 1259
 Haardt F., Madau P., 2012, *ApJ*, 746, 125
 Herbst E., 2001, *Chem. Soc. Rev.*, 30, 168
 Hindmarsh A. C., 1983, *Sci. Comput.*, 1, 55
 Hollenbach D., McKee C. F., 1979, *ApJS*, 41, 555
 Hopkins P. F., 2015, *MNRAS*, 450, 53
 Hopkins P. F., Narayanan D., Murray N., 2013, *MNRAS*, 432, 2647
 Hopkins P. F., Kereš D., Oñorbe J., Faucher-Giguère C.-A., Quataert E., Murray N., Bullock J. S., 2014, *MNRAS*, 445, 581
 Hopkins P. F. et al., 2018, *MNRAS*, 480, 800
 Hu C.-Y., Naab T., Walch S., Moster B. P., Oser L., 2014, *MNRAS*, 443, 1173
 Hu C.-Y., Naab T., Walch S., Glover S. C. O., Clark P. C., 2016, *MNRAS*, 458, 3528
 Hu C.-Y., Naab T., Glover S. C. O., Walch S., Clark P. C., 2017, *MNRAS*, 471, 2151
 Iwamoto K., Brachwitz F., Nomoto K., Kishimoto N., Umeda H., Hix W. R., Thielemann F.-K., 1999, *ApJS*, 125, 439
 Jiménez N., Tissera P. B., Matteucci F., 2014, *Mem. Soc. Astron. Ital.*, 85, 325
 Jiménez N., Tissera P. B., Matteucci F., 2015, *ApJ*, 810, 137
 Jura M., 1975, *ApJ*, 197, 575
 Katz H., Kimm T., Sijacki D., Haehnelt M., 2017, *MNRAS*, 468, 4831
 Kennicutt R. C., Jr, 1989, *ApJ*, 344, 685
 Kennicutt R. C., Jr, 1998, *ApJ*, 498, 541
 Kennicutt R. C., Jr et al., 2007, *ApJ*, 671, 333
 Krumholz M. R., Gnedin N. Y., 2011, *ApJ*, 729, 36
 Krumholz M. R., McKee C. F., 2005, *ApJ*, 630, 250
 Krumholz M. R., McKee C. F., Tumlinson J., 2009, *ApJ*, 699, 850
 Krumholz M. R., Dekel A., McKee C. F., 2012, *ApJ*, 745, 69
 Kuhlen M., Krumholz M. R., Madau P., Wise J., Smith B. D., 2011, *ApJ*, 749, 36
 Larson R. B., 1981, *MNRAS*, 194, 809
 Latif M. A., Schleicher D. R. G., 2015, *MNRAS*, 449, 77
 Latif M. A., Lupi A., Schleicher D. R. G., D'Amico G., Panci P., Bovino S., 2019, *MNRAS*, 485, 3352

- Leroy A. K., Walter F., Brinks E., Bigiel F., de Blok W. J. G., Madore B., Thornley M. D., 2008, *AJ*, 136, 2782
- Leroy A. K. et al., 2013, *AJ*, 146, 19
- Lupi A., Bovino S., 2020, *MNRAS*, 492, 2818
- Lupi A., Bovino S., Capelo P. R., Volonteri M., Silk J., 2018, *MNRAS*, 474, 2884
- Mac Low M.-M., Glover S. C. O., 2012, *ApJ*, 746, 135
- Maio U., Dolag K., Ciardi B., Tornatore L., 2007, *MNRAS*, 379, 963
- Maio U., Ciardi B., Dolag K., Tornatore L., Khochfar S., 2010, *MNRAS*, 407, 1003
- Maiolino R. et al., 2008, *A&A*, 488, 463
- Marri S., White S. D. M., 2003, *MNRAS*, 345, 561
- Matteucci F., Recchi S., 2001, *ApJ*, 558, 351
- McKee C. F., Krumholz M. R., 2010, *ApJ*, 709, 308
- McKee C. F., Ostriker E. C., 2007, *ARA&A*, 45, 565
- Micic M., Glover S. C. O., Federrath C., Klessen R. S., 2012, *MNRAS*, 421, 2531
- Mosconi M. B., Tissera P. B., Lambas D. G., Cora S. A., 2001, *MNRAS*, 325, 34
- Navarro J. F., Frenk C. S., White S. D. M., 1996, *ApJ*, 462, 563
- Nickerson S., Teyssier R., Rosdahl J., 2018, *MNRAS*, 479, 3206
- Nickerson S., Teyssier R., Rosdahl J., 2019, *MNRAS*, 484, 1238
- Omukai K., 2000, *ApJ*, 534, 809
- Pallottini A., Ferrara A., Bovino S., Vallini L., Gallerani S., Maiolino R., Salvadori S., 2017, *MNRAS*, 471, 4128
- Pilbratt G. L. et al., 2010, *A&A*, 518, L1
- Pineda J. L., Goldsmith P. F., Chapman N., Snell R. L., Li D., Cambrésy L., Brunt C., 2010, *ApJ*, 721, 686
- Plat A., Charlot S., Bruzual G., Feltre A., Vidal-García A., Morisset C., Chevillard J., Todt H., 2019, *MNRAS*, 490, 978
- Price D. J., 2008, *J. Comput. Phys.*, 227, 10040
- Richings A. J., Schaye J., 2016a, *MNRAS*, 458, 270
- Richings A. J., Schaye J., 2016b, *MNRAS*, 460, 2297
- Richings A. J., Schaye J., Oppenheimer B. D., 2014a, *MNRAS*, 440, 3349
- Richings A. J., Schaye J., Oppenheimer B. D., 2014b, *MNRAS*, 442, 2780
- Robertson B. E., Kravtsov A. V., 2008, *ApJ*, 680, 1083
- Safranek-Shrader C. et al., 2017, *MNRAS*, 465, 885
- Saintonge A. et al., 2017, *ApJS*, 233, 22
- Salpeter E. E., 1955, *ApJ*, 121, 161
- Sánchez-Blázquez P. et al., 2014, *A&A*, 570, A6
- Scannapieco C., Tissera P. B., White S. D. M., Springel V., 2005, *MNRAS*, 364, 552
- Scannapieco C., Tissera P. B., White S. D. M., Springel V., 2006, *MNRAS*, 371, 1125
- Scannapieco C., Tissera P. B., White S. D. M., Springel V., 2008, *MNRAS*, 389, 1137
- Schmidt M., 1963, *ApJ*, 137, 758
- Schmidt M., Wilson M., Observatories P., 1959, *ApJ*, 129, 16
- Schneider R., Omukai K., Inoue A. K., Ferrara A., 2006, *MNRAS*, 369, 1437
- Schruba A. et al., 2011, *AJ*, 142, 37
- Schuster K. F., Kramer C., Hirschfeld M., Garcia-Burillo S., Mookerjee B., 2007, *A&A*, 461, 143
- Seifried D., Sánchez-Monge Á., Suri S., Walch S., 2017, *MNRAS*, 467, 4467
- Semenov V. A., Kravtsov A. V., Gnedin N. Y., 2016, *ApJ*, 826, 200
- Sharda P., Krumholz M. R., Federrath C., 2019, *MNRAS*, 490, 513
- Shen S., Wadsley J., Stinson G., 2010, *MNRAS*, 407, 1581
- Shen S., Madau P., Guedes J., Mayer L., Prochaska J. X., Wadsley J., 2013, *ApJ*, 765, 89
- Shull J. M., et al., 2021, *ApJ*, 911, 55
- Solomon P. M., Rivolo A. R., Barrett J., Yahil A., 1987, *ApJ*, 319, 730
- Springel V., 2005, *MNRAS*, 364, 1105
- Springel V., Hernquist L., 2003, *MNRAS*, 339, 289
- Stecher T. P., Williams D. A., 1967, *ApJ*, 149, L29
- Sternberg A., Le Petit F., Roueff E., Le Bourlot J., 2014, *ApJ*, 790, 10
- Strong A. W., Mattox J. R., 1996, *A&A*, 308, 21
- Tielens A. G. G. M., Hollenbach D., 1985, *ApJ*, 291, 722
- Tissera P. B., Pedrosa S. E., Sillero E., Vilchez J. M., 2016a, *MNRAS*, 456, 2982
- Tissera P. B., Machado R. E. G., Sánchez-Blázquez P., Pedrosa S. E., Sánchez S. F., Snaith O. N., Vilchez J. M., 2016b, *A&A*, 592, A93
- Tomassetti M., Porciani C., Romano-Diaz E., Ludlow A. D., Papadopoulos P. P., 2014, *MNRAS*, 446, 3330
- Tricco T. S., Price D. J., 2013, *MNRAS*, 436, 2810
- Tumlinson J., 2002, *ApJ*, 566, 857
- Wakelam V. et al., 2017, *Molecular Astrophysics*, 9, 36,
- Weingartner J. C., Draine B. T., 2001, *ApJ*, 548, 296
- Williams J. P., McKee C. F., 1997, *ApJ*, 476, 166
- Wolfire M. G., McKee C. F., Hollenbach D., Tielens A. G. G. M., 2003, *ApJ*, 587, 278
- Wolfire M. G., Tielens A. G. G. M., Hollenbach D., Kaufman M. J., 2008, *ApJ*, 680, 384
- Wong T., Blitz L., 2002, *ApJ*, 569, 157
- Woosley S. E., Weaver T. A., 1995, *ApJS*, 55
- Yamasawa D., Habe A., Kozasa T., Nozawa T., Hirashita H., Umeda H., Nomoto K., 2011, *ApJ*, 735, 44

SUPPORTING INFORMATION

Supplementary data are available at *MNRAS* online.

Figure A: Face-on and edge-on maps (small panels) of the mass-weighted gas temperature (first column) and the projected surface density of SFR (second column), H_2 (third column) and HI (fourth) content in eZ (first row), eZ01 (second row), and eZ05 (third row).

Please note: Oxford University Press is not responsible for the content or functionality of any supporting materials supplied by the authors. Any queries (other than missing material) should be directed to the corresponding author for the article.

This paper has been typeset from a $\text{\TeX}/\text{\LaTeX}$ file prepared by the author.